

Effectiveness and nonlinear characterization of vibro-impact energy harvesting absorbers in controlling base-excited systems

Tyler Alvis and Abdessattar Abdelkefi*

Department of Mechanical and Aerospace Engineering, New Mexico State University, Las Cruces, NM, 88003, USA

Abstract

In this study, model derivations are carried out of a dynamical system under base excitations with a piezoelectric energy harvesting absorber as the tuned-mass-damper. Additionally, amplitude stoppers are included to the absorber in order to create a broadband resonant response, increasing the window of operational use for energy harvesting and system's control. This study is unique in the fact that the energy harvester is coupled to the source of its excitation. A nonlinear reduced-order model is developed using Euler-Lagrange principle and the Galerkin method to accurately estimate the energy harvesting absorber's displacement, harvested power, and the oscillating response of the primary structure. The nonlinear interaction of the energy harvesting absorber and the amplitude stoppers are the focus of this study, where an in-depth investigation of bifurcation points of the primary structure and energy harvesting absorber responses is performed. Due to a transfer of energy between the primary structure and the absorber, it is shown that a soft stopper with stiffness $5 * 10^3 N/m$ has great control of the primary structure with 60% of the uncontrolled amplitude being reduced, as well as an increase of the harvested energy. Medium stoppers with small initial gaps size and hard stoppers do not control the primary structure and show a decrease in the energy harvesting capabilities due to the activation of the nonlinear contact-impact interactions. These stoppers also generate aperiodic regions due to the possible presence of grazing bifurcations.

1. Introduction

One important consideration during the design process is the mitigation or control of harmful vibrations in dynamical systems due to environmental inputs [1, 2]. A common source of environmental vibrations is base excitations [3]. Base excitation can be harmful to a system when the forcing excitation frequency is almost equal to one of the natural frequencies of the primary structure, causing large harmonic oscillations [4]. To mitigate these dangerous harmonic oscillations, researchers proposed many strategies to control their systems including active and passive controllers [5]. Active controllers are commonly electronic systems that measure input vibrations and activate actuators to mitigate the wide range of input vibrations [6]. Passive controllers are systems that couple with the primary structure without the ability to adapt to the changing excitation frequencies [7]. Some passive controllers include tuned liquid column dampers, viscoelastic dampers, and most commonly, tuned-mass-dampers [8-10]. Tuned-mass-dampers are subsystems that couple its movement to the primary system, and its geometric and material parameters are tuned to eliminate the primary structure's

oscillations [11]. Since these parameters are constant, they are effective for only one forcing frequency, making them great for harmonic oscillations.

The most common tuned-mass-damper is a simple spring-mass-damper, but many types of tuned-mass-dampers have been investigated in the literature. One famous example of a pendulum tuned-mass-damper is seen in Taipei 101, one of the world's tallest buildings. Taipei 101 utilizes a 726 ton ball suspended from steel cables on the building's 92nd floor. When oscillations are low, the simple swinging motion of the pendulum is enough to control the building's motion. Additionally, the ball is attached to massive shock absorbers that help absorb the building's motion when the oscillations are high [12]. Another unique tuned-mass-damper is the particle tuned-mass-damper which utilizes the movement of a fluid or granular material that creates a damping effect due to the particles' momentum and the particles colliding with each other. Lu et. al. [13] performed experiments of a particle tuned-mass-damper effects on scaled building under varying seismic loads based on historical events. Their results proved that particle tuned-mass-dampers reduced the building's oscillations and acceleration under onsite earthquake excitations and artificial waves, especially when the excitation matched the natural frequency of the building.

As seen in the previous examples, most tuned-mass-dampers dissipate the primary system's kinetic energy mechanically. By converting the system's kinetic energy into electrical energy, small sensors and electrical components can be powered in remote locations, eliminating the need for lengthy or dangerous battery replacements [14]. There are many transduction mechanisms that harvest energy including electrostatic [15], electromagnetic [16,17], and piezoelectric [18]. Piezoelectric transduction mechanism is a popular mode of transduction as it has less complex parts as the other mechanisms, as it commonly is piezoelectric layers adhered to other substrate structures. Therefore, a piezoelectric energy harvester was utilized as a tuned-mass-damper in few previous studies [19-22]. Abdelmoula et al. [23] showed that piezoelectric energy harvesters can achieve both control of the primary system as well as energy harvested for systems under base excitation. Initially, a piezoelectric energy harvester was shown to efficiently control the primary structure's oscillations. They also focused on optimizing the piezoelectric energy harvesting absorber's load resistance and the thickness of the substrate to generate a broadband resonant response, hence harvesting high levels of power. McNeil et. al. [24] has also shown great primary system control with a system that is under base excitation and/or vortex-induced vibrations. The parametric values of the energy harvesting absorber were of particular interest, optimizing the absorber for both excitation sources. It was concluded that an absorber tuned for vortex-induced vibrations provided the best control and most even power output over the range of base excitations and wind speeds.

This study aims to further the work of energy harvesting absorbers by including amplitude stoppers to the energy harvester. The inclusion of amplitude stoppers can generate a nonlinear response from the contact between the stoppers and the energy harvesting absorber, which aims to broaden the operable range of

frequencies to harvest energy. In a recent study, Zhou et. al. [25] showed experimentally that the inclusion of amplitude stoppers to a piezoelectric energy harvester under base excitation generated a hardening effect that at least doubled the operable range of the energy harvester. The material of the stoppers affected this hardening effect, so the material and stiffness of the stoppers were investigated and optimized. This study differs from the work of Zhou et al. [25] due to the fact that the energy harvester acts as an absorber, and hence be directly coupled to the primary structure, and therefore influence its source of oscillation. An extensive study of the stopper's stiffness as well as the initial gap between the stoppers and the energy harvesting absorber is examined and discussed in this work. The rest of this work is organized as follows: in section 2, the primary system under consideration and the energy harvesting absorber are described. In addition, the nonlinear reduced-order model is developed. In section 3, the optimal design of the energy harvester absorber without the inclusion of the stoppers is selected. Then, results are shown in section 4 about the effect of the stoppers' hardness and gap as well as the possible nonlinear vibro-impact interactions between the energy harvesting absorber and the stoppers.

2. System's description and reduced-order modeling

To reduce high computational costs of running a high-fidelity model, a reduced-order model is used to represent the system. The coupled system under investigation is presented in Figure 1. The primary structure is represented as a simple spring-mass-damper system where the primary structure's stiffness k and damping coefficient c are denoted as a spring and damper, respectively. The primary structure's displacement is denoted by $w_1(t)$ and the base excitation the system is subjected to is represented as $y(t)$. The energy harvesting absorber consists of a steel substrate with two piezoelectric layers which partially cover the substrates length, and fully cover the substrates width. A tip mass is attached to the absorber's free end to tune the absorber's natural frequency. The absorber's relative displacement is denoted as $w_2(x,t)$, a function with respect to the distance along the beam and time. The absorber is represented as a continuous body using the Euler-Bernoulli beam theory and the Galerkin discretization method. The amplitude stoppers are indicated as the green hashed boxes.

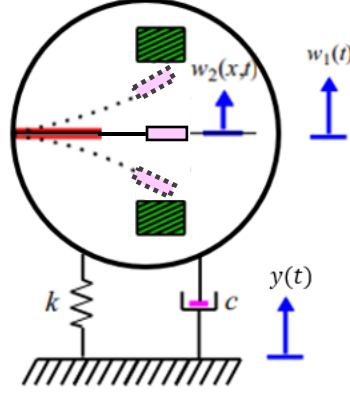


Figure 1: A representation of the coupled system under investigation.

To derive the reduced-order model's equations, the Euler-Lagrange equations are utilized. Therefore, the kinetic and potential energies, and the nonconservative work should be first expressed. These expressions are utilized in the Euler-Lagrange equations, which are given by:

$$\frac{d}{dt} \frac{\partial \ell}{\partial \dot{w}_1} - \frac{\partial \ell}{\partial w_1} = \frac{\delta W_{nc}}{\delta w_1} \quad (1)$$

$$\frac{d}{dt} \frac{\partial \ell}{\partial \dot{r}_i} - \frac{\partial \ell}{\partial r_i} = \frac{\delta W_{nc}}{\delta r_i} \quad (2)$$

$$\frac{d}{dt} \frac{\partial \ell}{\partial \dot{\lambda}} - \frac{\partial \ell}{\partial \lambda} = \frac{\delta W_{nc}}{\delta \lambda} \quad (3)$$

where the Lagrangian $\ell = T - \Pi$, T is the kinetic energy and Π represents the potential energy, $\dot{\lambda} = V$, and the nonconservative work W_{nc} .

The kinetic and potential energies can be expressed as follows:

$$T = \frac{1}{2} M \dot{w}_1^2 + \frac{1}{2} M_t \dot{u}^2 + \frac{1}{2} I_t \dot{w}_2(L,t)^2 + \frac{1}{2} M_{b1} \int_0^{L_1} (\dot{w}_1 + \dot{w}_2(x,t))^2 dx + \frac{1}{2} M_{b2} \int_{L_1}^L (\dot{w}_1 + \dot{w}_2(x,t))^2 dx \quad (4)$$

$$\Pi = \frac{1}{2} \int_{v_s} \sigma_x^s \varepsilon_x^s dv + \frac{1}{2} \int_{v_s} (\sigma_x^s \varepsilon_x^s - E_3 D_3) dv + \frac{1}{2} k (w_1 - y(t))^2 \quad (5)$$

where M is the mass of the primary structure, M_t is the mass of the tip mass, $\dot{u} = \dot{w}_1 + \dot{w}_2(L,t) + L_c \dot{w}_2'(L,t)$, the second moment of inertia, $I_t = \frac{4}{3} M_t L_c^2$, the mass of the beam, $M_{b1} = b \rho_s h_s + 2b \rho_p h_p$ and $M_{b2} = b \rho_s h_s$, the length of the substrate L , the length of the piezoelectric patch L_1 , the characteristic length of the tip mass L_c , and the electric displacement, $D_3 = d_3 E_p \varepsilon_x^p - \varepsilon_{33} E_3$.

As mentioned, the Galerkin discretization method, seen in equation 6, is used to develop a nonlinear reduced-order model of the energy harvesting absorber coupled to the primary structure. The Galerkin method considers the sum of the absorber's mode shapes times their positional coordinates. This allows the minimum numbers of modes to be used that accurately represents the system, optimizing the computational load of the

absorber. The process of solving for the energy harvester's mode shapes, φ_i , is known. Therefore, all details on the derivation of the energy harvester's mode shapes, their associated boundary conditions and orthogonality conditions is described in detail in [26]. The final expressions of the kinetic and potential energies after substituting the Galerkin discretization are expressed in equations 7 and 8.

$$w_2(x,t) = \sum_{i=1}^{\infty} \varphi_i(x)r_i(t) \quad (6)$$

T

$$\begin{aligned} &= \frac{1}{2}M\dot{w}_1^2 + \frac{1}{2}M_t\dot{u}^2 + \frac{1}{2}I_t \left(\sum_{i=1}^{\infty} \varphi_i'(x)\dot{r}_i(t) \right)^2 + \frac{1}{2}M_{b1} \\ &\int_0^{L_1} \left(\dot{w}_1 + \sum_{i=1}^{\infty} \varphi_i(x)r_i(t) \right)^2 dx + \frac{1}{2}M_{b2} \int_{L_1}^L \left(\dot{w}_1 + \sum_{i=1}^{\infty} \varphi_i(x)r_i(t) \right)^2 dx \end{aligned} \quad (7)$$

Π

$$\begin{aligned} &= EI_1 \int_0^{L_1} \left(\sum_i \varphi_i''(x)r_i(t) \right)^2 dx + EI_2 \int_{L_1}^L \left(\sum_i \varphi_i''(x)r_i(t) \right)^2 dx + be_{31}(h_s + h_p) \\ &\int_0^{L_1} \left(\sum_i \varphi_i''(x)r_i(t) \right) V(t) dx - \frac{e_{31}bL_1}{h_p} V(t)^2 + \frac{1}{2}k(w_1 - y(t))^2 \end{aligned} \quad (8)$$

where the energy harvesting absorber's stiffnesses, $EI_1 = bE_s \frac{h_s^3}{12} + \frac{1}{2}bE_p h_s^2 h_p + bE_p h_s h_p^2 + bE_p \frac{2}{3}h_p^3$ and $EI_2 = bE_s \frac{h_s^3}{12}$, and $\dot{u} = \dot{w}_1 + \sum_{i=1}^{\infty} \varphi_i(L)r_i(t) + L_c \sum_{i=1}^{\infty} \varphi_i'(L)r_i(t)$.

The system's nonconservative work comes from the primary structure's and the energy harvesting absorber's damping terms, as well as the excitation force and the contact force between the absorber and the stoppers. The expression of the variation of the nonconservative work can be written as:

$$\delta W_{nc} = -c(\dot{w}_1 - \dot{y}(t))\delta w_1 - \int_0^L c_a \left(\sum_{i=1}^{\infty} \varphi_i(x)r_i(t) \right) dx \delta w_2 - I\delta\lambda + F_{stoppers}\delta w_1 \quad (9)$$

where c_a represents the damping of the absorber, I is the current, the voltage generated $V = \dot{\lambda}$, and the force of the stopper $F_{stopper}$.

The force of the stopper is represented as a trilinear spring model. This model has been shown to adequately represent the contact force by Paidoussis et al. [27], and is expressed as:

$$F_{stopper} = k_s \left[\sum_{i=1}^{\infty} \varphi_i(L_s)r_i(t) - \frac{1}{2} \left(\left| \sum_{i=1}^{\infty} \varphi_i(L_s)r_i(t) + d \right| - \left| \sum_{i=1}^{\infty} \varphi_i(L_s)r_i(t) - d \right| \right) \right]^3 \quad (10)$$

where L_s denotes the distance along the beam where the stoppers are placed, d is the initial distance between the beam and the stoppers, k_s represents the stoppers' stiffness. Importantly, this model was also used in [28]

which computationally analyzed stoppers' effects on a piezoelectric energy harvester. This impact force represented with differing stiffnesses is depicted in Figure 2.

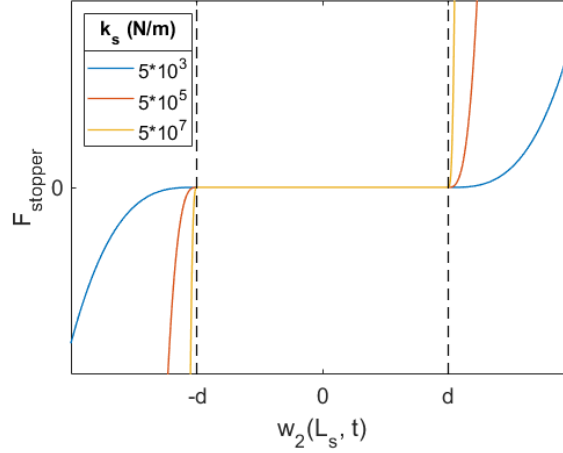


Figure 2: The force of the stopper versus the displacement of the absorber for varying stopper stiffnesses.

After substituting in the kinetic and potential energy, equations 7 and 8, and the nonconservative work, equation 9, into the Euler-Lagrange equations 1-3, the nonlinear reduced-order model can be expressed as:

$$M_{S1}\ddot{w}_1 + c\dot{w}_1 + kw_1 + \sum_{i=1}^{\infty} M_{S2i}\ddot{r}_i = F\cos(\omega_f t + \phi) \quad (11)$$

$$\ddot{r}_i + 2\xi_i\omega_i\dot{r}_i + \omega_i r_i + M_{S2i}\ddot{w}_1 - \theta_i V = \varphi_i(L_s)F_{stopper} \quad (12)$$

$$C_p\dot{V} + \frac{1}{R} + \sum_{i=1}^{\infty} \theta_i \dot{r}_i = 0 \quad (13)$$

where the capacitance of the harvester is $C_p = 2\frac{\varepsilon_{33}bL_1}{h_p}$, the piezoelectric coupling term is $\theta = E_p d_{31}b(h_p + h_s)\varphi'_i(L_1)$, and the two mass sums are as follows:

$$M_{S1} = M + M_t + M_{b1}L_1 + M_{b2}(L - L_1)$$

$$M_{S2i} = M_t\varphi_i(L) + M_t L_c \varphi'_i(L) + M_{b1} \int_0^{L_1} \varphi_i(x)dx + M_{b2} \int_{L_1}^L \varphi_i(x)dx$$

3. Optimal selection of energy harvesting absorber's dimensions

Once the equations of motion are developed, it is important to investigate the energy harvesting absorber's parameters effects on the overall performance of the coupled system and select the optimal design parameters of the absorber with the objective of simultaneously control the primary structure at resonance and maximize the harvested energy from the absorber. To reach this target, the coupled natural frequencies will be investigated through a linear eigenvalue analysis, as the imaginary eigenvalues are the coupled natural frequencies of the system. This analysis will aid selecting the harvester's dimensions in such a way that the

two coupled frequencies are close enough to each other and hence possible creating of ultra-wide bandwidth resonance. For this analysis, only one mode is used in the Galerkin discretization. The linearized system can be represented as:

$$\dot{\mathbf{z}} = \mathbf{A}\mathbf{z} \quad (14)$$

where \mathbf{z} represents the state space variables $\mathbf{z} = [w_1 \dot{w}_1 r_1 \dot{r}_1 V]^T$, and the matrix \mathbf{A} is described as:

$$\mathbf{A} = \begin{bmatrix} 0 & 1 & 0 & 0 & 0 \\ -\frac{k}{M_{s1} - M_{s21}^2} & -\frac{c}{M_{s1} - M_{s21}^2} & \frac{\omega_1^2 M_{s21}}{M_{s1} - M_{s21}^2} & \frac{2\xi\omega_1 M_{s21}}{M_{s1} - M_{s21}^2} & -\frac{\theta_1 M_{s21}}{M_{s1} - M_{s21}^2} \\ 0 & 0 & 0 & 1 & 0 \\ \frac{kM_{s21}}{M_{s1} - M_{s21}^2} & \frac{cM_{s21}}{M_{s1} - M_{s21}^2} & \frac{\omega_1^2 M_{s1}}{M_{s1} - M_{s21}^2} & \frac{2\xi\omega_1 M_{s1}}{M_{s1} - M_{s21}^2} & \frac{\theta_1 M_{s1}}{M_{s1} - M_{s21}^2} \\ 0 & 0 & 0 & -\frac{\theta_1}{C_p} & -\frac{1}{RC_p} \end{bmatrix}$$

During this analysis, the imaginary eigenvalues are plotted against the energy harvesting absorber's tip mass. This is because the tip mass has a large effect on the absorber's natural frequency, making it easy to identify which of the coupled natural frequencies is dominated by the absorber. Figure 3(a) shows the imaginary eigenvalues for varying substrate thicknesses, represented as the solid lines, overlaid with the energy harvesting absorber's uncoupled natural frequency, represented as the dashed lines. It can be seen that the natural frequency of the energy harvesting absorber matches the higher coupled natural frequency curve when the tip mass is equal to zero kilograms. This is also logical for small values of the tip mass which are negligible to the mass of the primary structure, and the lower coupled natural frequency is unaffected by the change in the tip mass of the energy harvesting absorber. Additionally, as the tip mass increases, the higher coupled natural frequency no longer follows the uncoupled natural frequency of the absorber. This is an evidence of the veering phenomenon. Indeed, the veering phenomenon occurs when two frequencies approach each other and then move apart without crossing. While they are close together, the two modes interact and hybridize. After the hybridization, the two modes continue on the path the other would have taken had the two modes crossed [29]. This can be seen in Figure 3(a) as the dashed lines represent the energy harvesting absorber's uncoupled natural frequency, clearly showing that hybridization occurs around 0.02 – 0.07 kg depending on the parametric value.

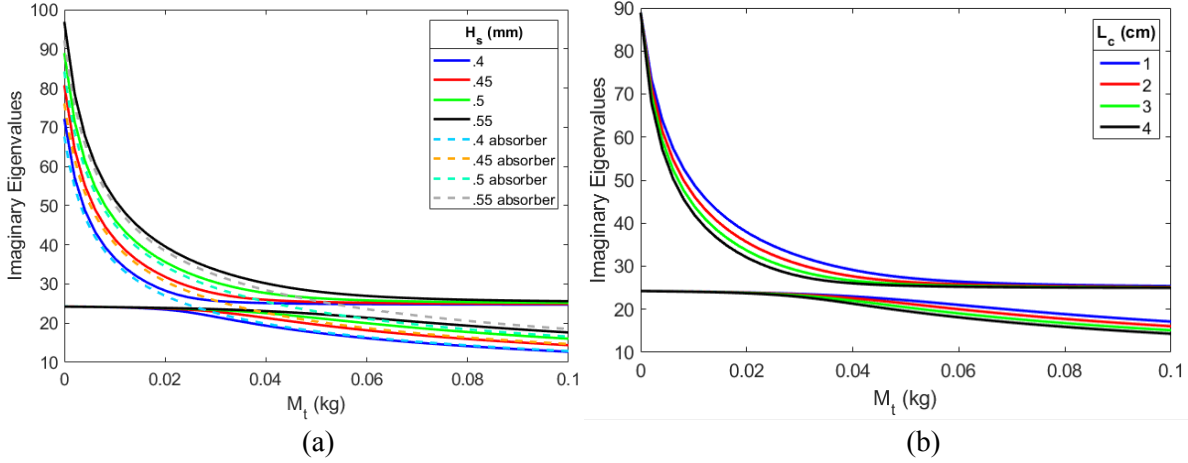


Figure 3: Eigenvalue analysis of the parameters: (a) the height of the substrate compared to the absorber's uncoupled natural frequency and (b) the characteristic length of the tip mass.

The difference between the two coupled natural frequencies are investigated to select the optimal parameters' values for the energy harvesting absorber. When this difference is small, a strong coupling of the natural frequencies is enforced, ensuring that the energy harvesting absorber may eliminate the primary structure's harmful oscillations and create a broadband resonance region. To select the optimal parameter values, the tip mass region from 0.04 kg to 0.05 kg is focused on. Since the parameters will all affect the system, focusing on a small range of tip masses will allow for all of the parameters to be selected where an optimal tip mass value for all parameters can be determined. Therefore, once the parameters' values are selected, the coupled system is studied without the use of stoppers to determine the optimal tip mass. The optimal tip mass is selected when the energy harvesting absorber is directly coupled to the primary structure's coupled natural frequency, resulting in two equal peaks centered around the primary structure's coupled natural frequency. If the coupled natural frequencies are not optimally tuned, the resulting peaks will not be centered around the primary structure's coupled natural frequency, resulting in one of the peaks to be large. When the peaks are equal, this ensures the primary structure's amplitude is minimized, as well as an optimal average power generated throughout the range of excitation frequencies. It is seen in Figure 4 that the optimal value of the tip mass for the current parameters is 0.048 kilograms . A full list of the parameter values can be seen in Table 1.

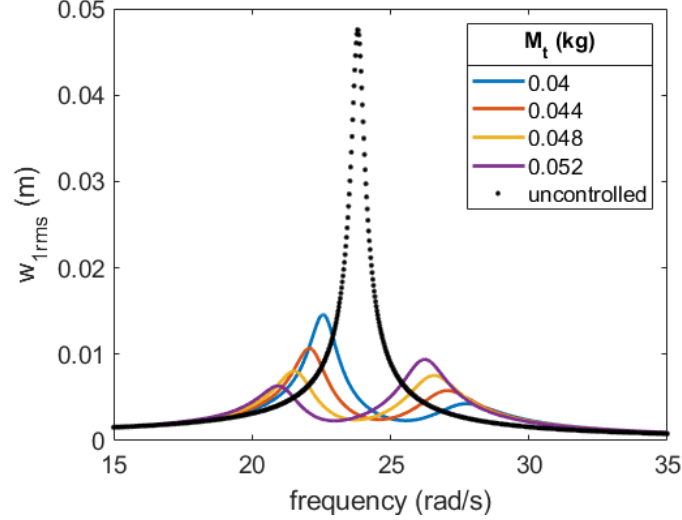


Figure 4: The tip mass effects on the primary structure's amplitude versus varying excitation frequencies.

Table 1: Reduced-order model's parametric values.

Parameter	Parameter Symbol	Parameter Value
Young's modulus of the absorber substrate	E_s	$190 * 10^9 N/m^2$
Young's modulus of the piezoelectric layers	E_p	$30.3366 * 10^9 N/m^2$
Height of the substrate	h_s	$0.5 mm$
Height of the piezoelectric layers	h_p	$0.267 mm$
Length of the substrate	L	$18 cm$
Length of the piezoelectric layers	L_1	$9 cm$
Characteristic length of the tip mass	L_c	$2 cm$
Width of the substrate and piezoelectric layers	b	$2 cm$
Density of the substrate	ρ_s	$7800 kg/m^3$
Density of the piezoelectric layers	ρ_p	$2730 kg/m^3$
Tip mass	M_t	$0.048 kg$
Mass of the primary structure	M	$1.2 kg$
Damping coefficient of the structure	c	$0.5879 Ns/m$
Damping ratio of the absorber	ξ	0.05
Stiffness of the primary structure	k	$720 N/m$
Piezoelectric strain coefficient	d_{31}	$-320 * 10^{-12} C/N$
Piezoelectric permittivity component	ϵ_{33}	$27.3 * 10^{-9} F/m$

4. Results and discussion

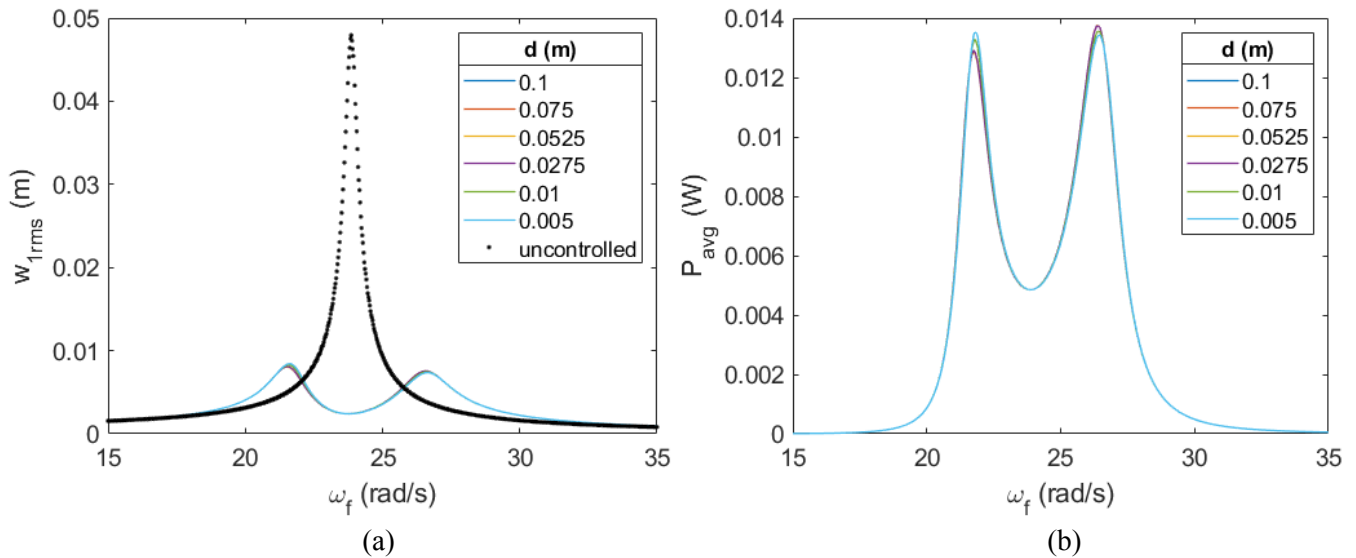
The two important characteristics of the coupled system that are studied is the control of the primary structure and the power generated from the energy harvesting absorber. The impacts of considering two symmetric identical stoppers on the effectiveness of the coupled system are examined. Indeed, different stoppers' stiffness and initial stoppers' gap are investigated. Additionally, the peak power, average power, and the bandwidth of the power are determined to find the most optimal design in relation with the stoppers design. The stoppers' stiffnesses are categorized based on their relative stiffness to soft, medium, and hard. The

relationship between the stoppers' category and its gap to the energy harvesting absorber is identified in this section and the optimal stoppers design (gap and stiffness) for each category is determined. In addition, the influences of the stoppers' hardness of the vibro-impact behavior of the energy harvesting absorber are deeply studied by identifying possible bifurcations in the responses of the absorber.

4.1. Effects of the stopper's hardness and initial gap on the coupled system's effectiveness

4.1.1. Coupled system's performance under soft stoppers configuration

The stiffnesses chosen for the soft stoppers are $5 \times 10^2 \text{ N/m}$ and $5 \times 10^3 \text{ N/m}$, and their effects on the coupled system effectiveness can be seen in the frequency response functions of the primary structure root mean square (RMS) displacement and average harvested power of the energy harvesting absorber, as shown Figure 5. Inspecting the plotted curves in Figures 5(a) and 5(b), it is clear that a stoppers' stiffness of $5 \times 10^2 \text{ N/m}$ has a negligible effect on the coupled system's performance. In fact, the primary structure and harvested power frequency response functions are almost the same even when the initial gap between the stopper and absorber is very small. As the purpose of the amplitude stoppers is to generate an improved broadband resonance region and/or enhance the levels of the harvested power, this stopper's stiffness will not be considered in future analyses. As for the frequency response function of the stoppers' stiffness of $5 \times 10^3 \text{ N/m}$ shown in Figures 5(c) and 5(d), it can be noted that promising enhancement in the level of the harvested power as well as the broadband region is achieved. With the smallest gap of 0.005 m , the energy harvesting absorber has controlled 62% of the primary structure's uncontrolled amplitude. When looking at the generated power in Figure 5(d), the peak power increases with decreasing gap size. Additionally, the left peak has a slight nonlinear hardening, increasing the average power more than if there was no hardening and just a simple increase.



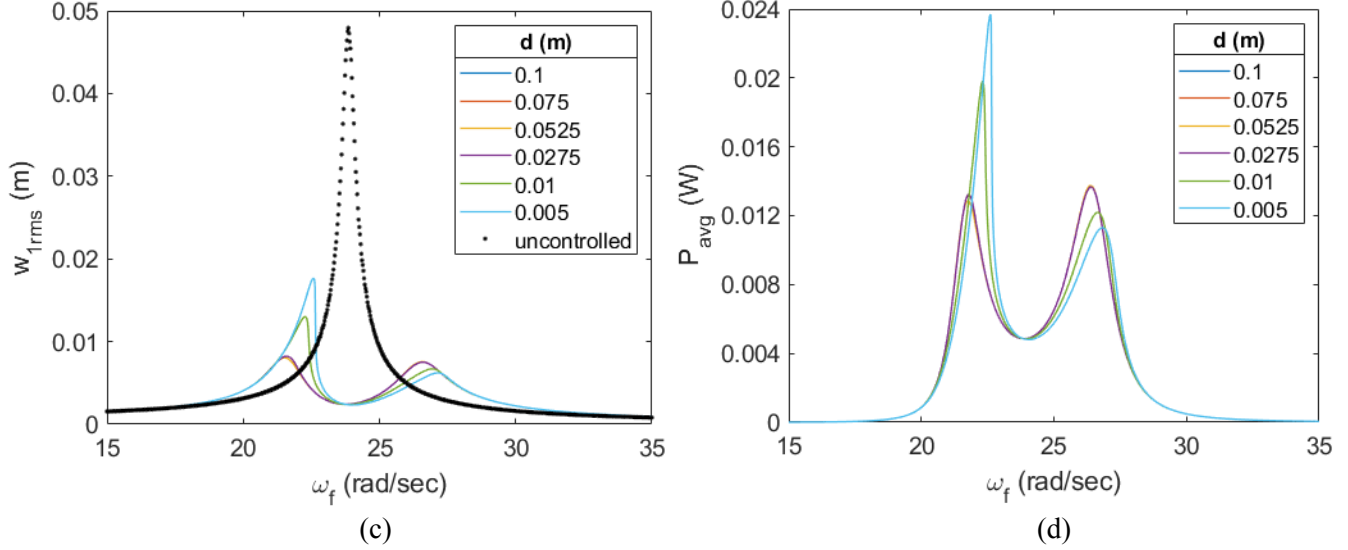


Figure 5: Soft absorber's effects on (a, c) primary structure displacement and (b, d) power generated with a stiffness of (a, b) $5 * 10^2 N/m$ and (c, d) $5 * 10^3 N/m$.

Figure 6 investigates the time histories of the primary structure and the energy harvesting absorber at the onset of excitation for stoppers with a stiffness of $5 * 10^3 N/m$ at a forcing frequency of $22.31 rad/s$. Figure 6(b) shows the energy harvesting absorber's transient time history with dashed lines that represent the location of the stoppers with corresponding colors to its gap size. It can be seen that the coupling between the primary and absorber systems causes a pumping effect to occur. This is seen at the beginning of the time histories where one of the coupled systems is large, while the other is small. The system with the larger amplitudes excites the other, thus pumping the overall system's amplitude up. Interestingly, the soft stoppers' stiffness does not have an initial impact on the energy harvesting absorber's amplitude compared to the gap size of $0.0525 m$, which is the case where there is no impact with the stoppers. The decreasing stopper size is causing the frequency of the absorber to increase slightly, but the force of the stoppers on the coupled system increases the amplitude of the primary structure. When looking at the steady-state response of the absorber in Figure 6(d), the increase in frequency becomes clear. Additionally, the steady-state amplitudes are shown, signifying the stoppers effects on the coupled system.

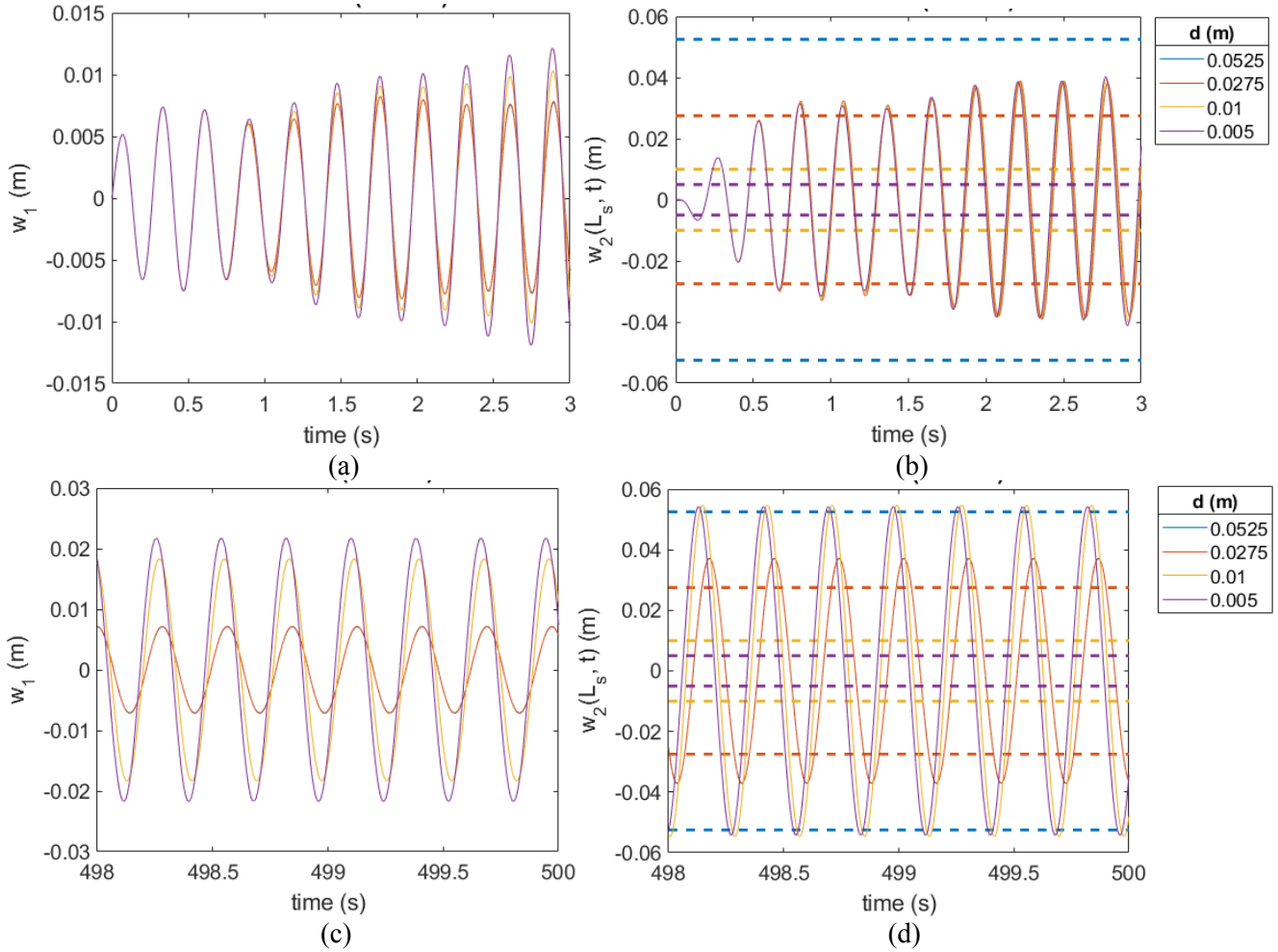


Figure 6: Transient (a, b) and steady-state (c, d) time histories of the (a, c) primary structure, and (b, d) the energy harvesting absorber showing the coupled system excitation stoppers with a stiffness of $5 * 10^3 N/m$ at a forcing frequency of 22.31 rad/s.

Table 2 contains in depth data for the soft stoppers' configuration and all initial gaps, allowing the comparison to a coupled system without stoppers. A case without stoppers can be seen in the first line where there is a gap of 0.1 m to 0.0525 m, as these gaps are too large to induce contact with the energy harvesting absorber. The bandwidth is investigated at a common power response to easily compare the different configurations. The stoppers with stiffness $5 * 10^2 N/m$ have nearly no effect on the system's response, with only a 0.5% difference the control of the primary structure's amplitude. A stopper stiffness of $5 * 10^3 N/m$ and a gap size of 0.005 m has a peak power that is nearly twice as large as the case without stoppers. Additionally, there is only a difference of 1% between the average powers of gap sizes of 0.01 m and 0.005 m. This is due to the hardening effects, seen in Figure 5(d), of the first peaks being nearly identical in the two cases. Also, the second peak decreases less for a gap size 0.01 m than it does for a gap size of 0.005 m. This indicates that a gap size of 0.01 m is a great candidate for system's that require more control of the primary system without sacrificing a large amount of harvested power. It is noted that all configurations of the soft

stoppers have the same bandwidth. This is due to the measurement being taken at a power of 0.004 W , but the change in bandwidth would be nearly insignificant. 0.004 W was chosen for this measurement to help compare these results to the medium and hard stoppers configurations where broader bandwidths are present.

Table 2: Performance analysis of the energy harvesting absorber for soft stoppers configuration.

Gap size (m)	Stiffness (N/m)	Peak power (W)	Average power (W)	Bandwidth of energy harvested (rad/s @ Power W)	Percent of amplitude controlled
0.1-0.0525	All	0.0138	0.00250	6.84 @ 0.004	83.1
0.01-0.005	$5 * 10^2$	≈ 0.0135	0.00250	6.84 @ 0.004	82.7-82.3
0.0275	$5 * 10^3$	0.0137	0.00251	6.84 @ 0.004	82.7
0.01		0.0198	0.00258	6.84 @ 0.004	72.7
0.005		0.0237	0.00261	6.84 @ 0.004	62.0

4.1.2. Coupled system's performance under medium stoppers configuration

The stiffnesses chosen for the medium stoppers are $5 * 10^4\text{ N/m}$ and $1 * 10^5\text{ N/m}$, and their effects on the levels of the harvested power as well as the primary structure oscillations are presented in Figure 7. It follows from the frequency response functions that these two stoppers' stiffnesses show very similar results. A gap size of 0.0275 m shows good control of the primary structure's amplitude, controlling 65% and 60% for the different stiffnesses, respectively. Additionally, a gap of 0.0275 m shows an increase in the peak average power compared to the cases where no contact occurs. However, smaller gaps of 0.01 m and 0.005 m only control 18% and 13%, respectively, for stoppers' stiffness of $5 * 10^4\text{ N/m}$. It is apparent that small gaps of 0.01 m and 0.005 m begin to see impact effects from the stoppers due to the higher values of the stoppers' stiffness compared to soft stoppers' configurations. Further, it can be seen that a broadband resonance region is forming with the small gaps which extends past the original operable range. This broadband region is generated from the onset of an aperiodic region. This region can be easily seen in Figure 7(d), at a forcing frequency of 26 rad/s where a sharp decrease occurs, followed by some noise as the average power increases. This noise is a result of the root mean square function averaging out the values of the aperiodic values. An in-depth analysis of these nonlinear effects and aperiodic regions are performed in the Section 4.2. Though a broadband region is a wanted effect of the amplitude stoppers, it is also apparent that the first peaks are also seeing a nonlinear hardening effect, shifting to the right. This shift is close to the additional frequencies obtained from the broadband region, thus negating the benefits of the broadband region. When this is included with the fact that the overall peak power is decreased, gaps like 0.0275 m where there are no extreme nonlinear effects are preferable for medium stoppers. It should be also mentioned that a strong coupling between the vibro-impact dynamics of the absorber with the stoppers leads to an activation of the primary structure oscillations and hence the presence of the nonlinear hardening effects and hence an increase in the harvested power for the first resonant peak of the coupled system.

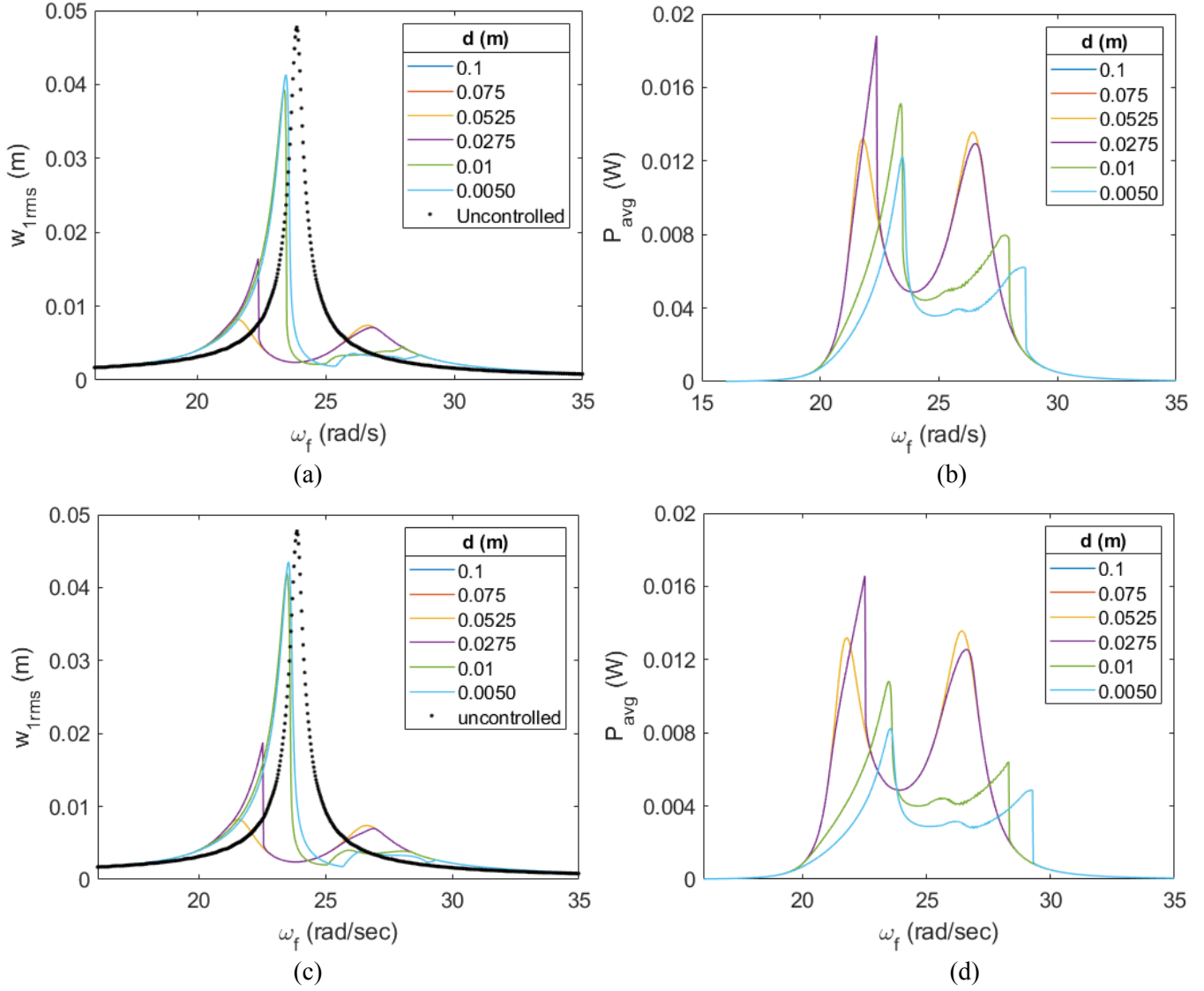


Figure 7: Medium stoppers' effects on (a, c) primary structure and (b, d) power generated with a stiffness of (a, b) $5 * 10^4 N/m$ and (c, d) $1 * 10^5 N/m$.

The stoppers' effects on the excitation of the coupled system with stoppers of stiffness $5 * 10^4 N/m$ at a forcing frequency of $22.37 rad/s$ can be seen in Figure 8. It can be noted in the small gaps that the stoppers significantly affect the amplitude of the energy harvesting absorber. Since the absorber comes into contact with the stoppers with small gaps almost immediately, it begins to excite the primary structure, and further pumps the absorber to have an increasing amplitude as well.

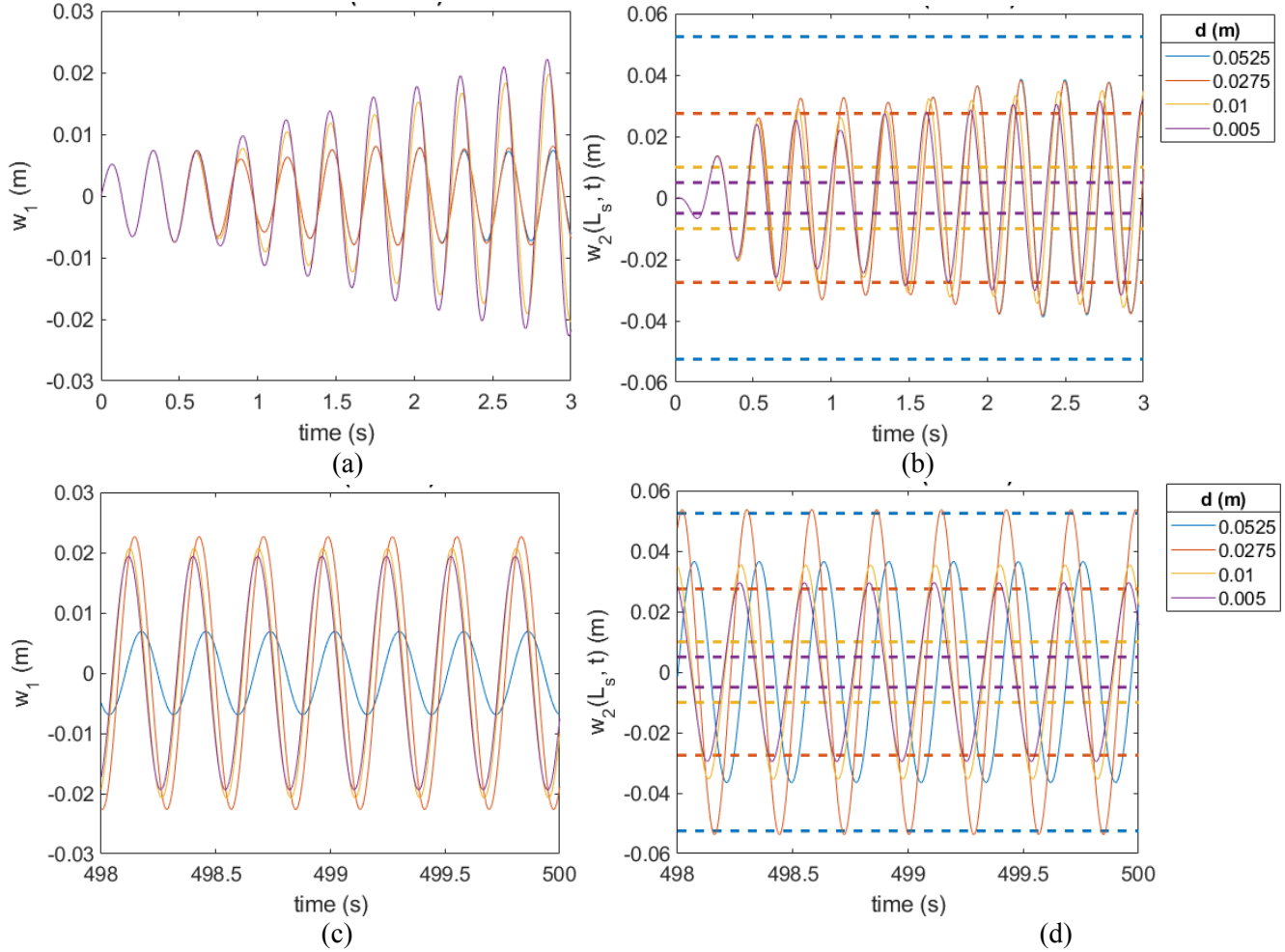


Figure 8: Transient (a, b) and steady state (c, d) time histories of the (a, c) primary structure, and (b, d) the energy harvesting absorber showing the coupled system excitation for stoppers with a stiffness of $5 * 10^4 N/m$ at a forcing frequency of 22.37 rad/s .

Table 3 contains in depth data for the medium stoppers' configuration and all initial gaps. When compared to the soft stoppers with stiffness $5 * 10^3 N/m$ and a gap size of 0.01 m depicted in Table 2, stoppers with a stiffness of $5 * 10^4 N/m$ and a gap size of 0.0275 m has a slightly lower peak and average power, being 5% and 0.39% smaller, respectively. However, the stopper stiffness of $5 * 10^3 N/m$ with a gap of 0.01 m controls 7.2% more of the primary structure than a stiffness of $5 * 10^4 N/m$ with a gap of 0.0275 m , indicating the soft stoppers configuration performs better on all fronts than that of the medium stoppers. Even though the nonlinear interaction of small gaps creates an expansion of the bandwidth, the overall bandwidth decreases by 1.75% to 14% depending on the configuration. This is due to the nonlinear hardening seen in the first peak, which negates the expansion of the second peak. Additionally, the peak and average power are much lower for these configurations, as well as a drastic decrease in the energy harvesting absorber's ability to control the primary structure's oscillations.

Table 3: Performance analysis of the energy harvesting absorber for medium stoppers configuration.

Gap size (m)	Stiffness (N/m)	Peak power (W)	Average power (W)	Bandwidth of energy harvested (rad/s @ Power W)	Percent of amplitude controlled
0.1-0.0525	all	0.0138	0.00250	6.84 @ 0.004	83.1
0.0275	5 * 10 ⁴	0.0188	0.00257	6.84 @ 0.004	65.5
0.01		0.0151	0.00206	6.57 @ 0.004	17.7
0.005		0.0122	0.00171	6.72 @ 0.004	13.4
0.0275	1 * 10 ⁵	0.0166	0.00253	6.84 @ 0.004	60.7
0.01		0.0108	0.00171	6.64 @ 0.004	12.0
0.005		0.0082	0.00135	5.86 @ 0.004	8.8

4.1.3. Coupled system's performance under hard stoppers configuration

As for the hard stoppers' configuration, two distinct stoppers' stiffnesses are, namely, $5 * 10^5 N/m$ and $5 * 10^7 N/m$. The frequency response functions of the primary structure and harvested power are presented in Figure 9. A gap of 0.0275 m and stoppers' stiffness of $5 * 10^5 N/m$ shows adequate control of the primary structure's amplitudes by controlling 53% of the uncontrolled case. However, the stiffness of $5 * 10^7 N/m$ shows little control of the primary structure regardless of the gap sizes that induce contact with the absorber. For instance, a gap of 0.0275 m only controls 23% of the uncontrolled amplitudes. Also, the generated power is no longer increasing due to contacting the stoppers. This is drastic when looking at a stiffness of $5 * 10^7 N/m$, where a gap size of 0.0275 m plateaus around 0.006 W. It can also be seen, even with the increased stiffnesses, both cases of 0.0275 m still do not show a wider broadband region even though an aperiodic region is present in the second peak, where the cases of smaller gaps do generate a broadband region. Additionally, aperiodic regions are present in the first peaks of the average power as well as the second. The broadband regions become broader with decreasing gap sizes, however the average power is also greatly decreasing and the primary structure may not be controlled as expected. It should be noted that the nonlinear coupling between the vibro-impact motion of the absorber and the stoppers results in strengthening the primary structure motion and hence the nonlinear hardening effects. This results in an inefficient control of the primary system motion in addition to the reduction of the harvested power due to the hardness of the stopper and smaller gap.

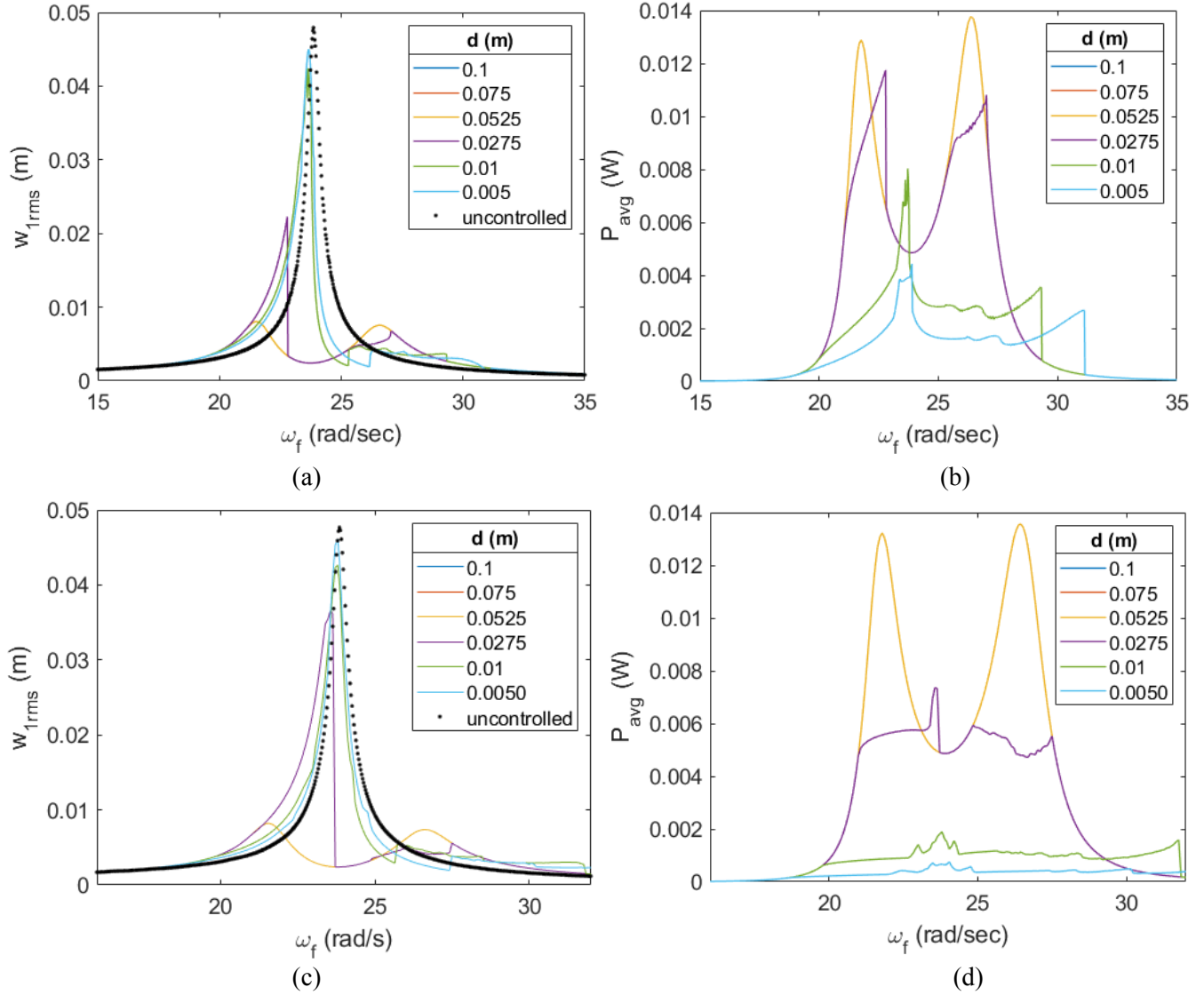


Figure 9: Hard stoppers' effects on (a, c) primary structure and (b, d) power generated with a stiffness of (a, b) $5 * 10^5 N/m$ and (c, d) $5 * 10^7 N/m$.

Figure 10 shows the onset of excitation for the coupled system with stoppers of stiffness $5 * 10^7 N/m$ and an excitation frequency of $23.56 rad/s$. With the given stiffness and small gap sizes, the pumping cannot be seen. When the gap sizes are small, the absorber does not come close to the amplitude when the gap is large enough to not induce contact. This implies that the strong stiffness of the stoppers' does not allow the absorber to fully couple with the primary structure, thus eliminating the absorber's ability to control the motion of the primary structure. It is noted that the system with a gap size of $0.0275 m$ just barely comes into contact with the stoppers, where the maximum amplitude of the case with large gaps reaches an amplitude of $0.036 m$. However, the hard impact force of this stiffness causes the pumping between the coupled systems to keep the absorber coming into contact with the stoppers. As the absorber is dissipating most of its energy away before

coming into contact with the stoppers, the primary structure's amplitude only increases slightly when compared to the increases due to the cases with smaller gaps. Additionally, a gap of 0.005 m induces an aperiodic response of the absorber immediately, and the presence of grazing bifurcations can also be seen. The steady-state response of the energy harvesting absorber (Figure 10(d)) shows that the hard stiffness of the stoppers affects all of the cases where there is contact with the stoppers. A gap of 0.0275 m appears to be periodic, however it has some complex behavior.

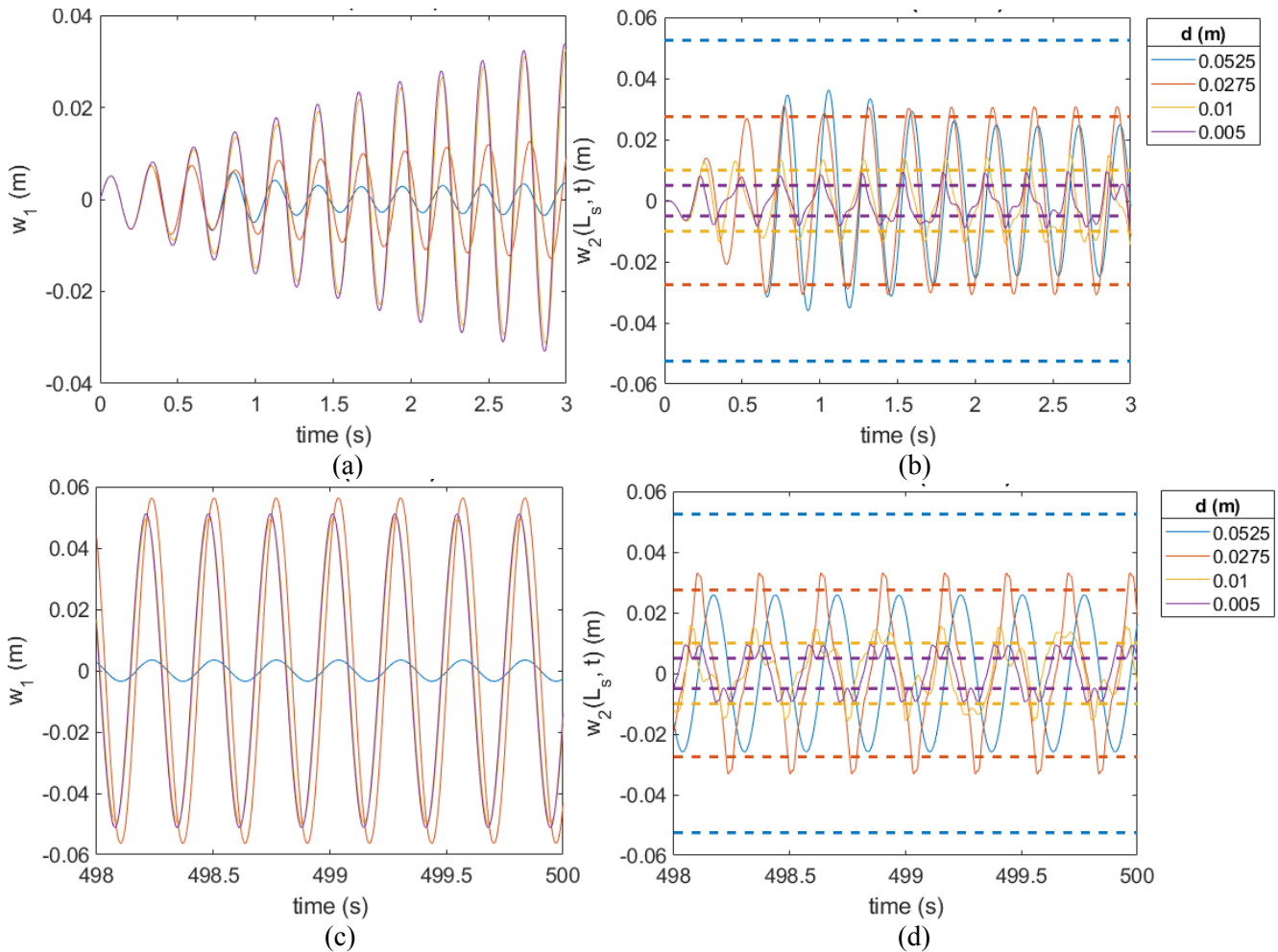


Figure 10: Transient (a, b) and steady state (b, d) time histories of the (a, c) primary structure, and (b, d) the energy harvesting absorber showing the coupled system excitation for stoppers with a stiffness of $5 * 10^7\text{ N/m}$ at a forcing frequency of 23.56 rad/s .

A complete data analysis for the hard stoppers' configuration can be seen in table 4. It is clear that the stoppers have a large impact on the power generated and the control of the primary structure. For both stiffnesses of the hard stoppers, a decrease in the harvested power is seen whenever there is contact with the stoppers. This decrease is extreme for cases with small gap sizes where broadband regions are present. To help analyze the bandwidth, the gaps where no contact is present are evaluated at the same harvested power as the smaller gaps. When investigating the bandwidth of the response, it is clear that when there is a nonlinear

response causing an increase or decrease in bandwidth that the primary system is not being controlled, with no cases controlling more than 12%. The largest broadband region seen is that of a stopper stiffness of $5 * 10^7$ N/m with a gap of 0.005 m with a region that is 33% larger than the case with no stoppers at the same power level. However, the power generated is miniscule and it only controls 3.3% of the primary structure's amplitude. The hard stoppers configuration does not achieve the design goal of the amplitude stoppers.

Table 4: Performance analysis of the energy harvesting absorber for hard stoppers configuration.

Gap size (m)	Stiffness (N/m)	Peak power (W)	Average power (W)	Bandwidth of energy harvested (rad/s @ Power W)	Percent of amplitude controlled
0.1-0.0525	all	0.0138	0.00250	7.21 @ 0.003 9.95 @ 0.0006 13.3605 @ 0.00016	83.1
0.0275	$5 * 10^5$	0.0117	0.00233	7.21 @ 0.003	53.3
0.01		0.008	0.00115	6.91 @ 0.003	11.1
0.005		0.0044	0.00083	7.88 @ 0.003	5.7
0.0275	$5 * 10^7$	0.0074	0.00175	9.95 @ 0.0006 13.3605 @ 0.00016	23.4653
0.01		0.0019	0.00054	11.89 @ 0.0006	10.6
0.005		0.0008	0.00026	17.55 @ 0.00016	3.3

4.2. Nonlinear characterization of vibro-impact energy harvesting absorber

Based on the presented results in the previous section, it is clear that the presence of the stoppers may result in the appearance of aperiodic responses due to the discontinuous behaviors in the frequency response functions of the RMS structural displacement and average harvested power. To understand the causes behind these aperiodic responses and to characterize the possible existence of bifurcations due to the presence of the stoppers, all peak values of the energy harvesting absorber displacement and its interaction with the stoppers are investigated from a bifurcation analysis perspective. Furthermore, the energy harvesting absorber's time histories, phase portraits, power spectra, and Poincare maps are determined in order to accurately identify the response periodicity (period- n , quasi-periodic, chaotic, etc) and to characterize the existing bifurcations. Time histories and the phase portraits are great tools to show the absorber's interaction with the amplitude stoppers and indicating the cause of any bifurcations. Indeed, grazing bifurcation can be qualitatively identified when inspecting the time histories and phase portraits of the energy harvesting absorber.

It should be mentioned due to the presence of the contact/impact boundaries of the stoppers, grazing bifurcations may take place. Grazing bifurcation occurs in periodic orbits contacting a boundary tangentially with zero velocity [30]. The time histories are also sufficient to characterize the behavior for low-order periodic responses. If the time history is uniform and has a harmonic period cycle of one period, the system's response is of period-1 [31]. For higher-order periodic responses of period- n , the power spectrum can easily identify the number of periods. The power spectrum contains peaks of the forcing frequency Ω and $\frac{k\Omega}{n}$, where k is an integer

and n represents the number of periods. Power spectrum has its limits when the system behaves more aperiodically, making it difficult to determine if the system is behaving quasi-periodically or chaotically, so Poincare maps should be employed. Poincare maps have n distinct points when the system is behaving with period- n . Additionally, if there are an infinite number of points forming a closed loop, the system is behaving quasi-periodically. The system is behaving chaotically when there are an infinite number of points which do not form a closed loop. Only medium and hard stoppers are investigated and deeply characterized as the soft stoppers do not show nonlinear aperiodic responses.

4.2.1. Energy harvesting absorber's nonlinear characterization under medium stoppers configuration

A stiffness of $5 * 10^4 N/m$ and a gap size of $0.01 m$ medium stoppers' configuration is selected in order to explore the interaction between the energy harvesting absorber and the stoppers. Figure 11 shows the bifurcation diagram of the energy harvesting absorber's motion and the stoppers' locations marked with the black dashed lines. This bifurcation diagram expresses the behavior of the absorber, as each dot represents a peak in the time history. Like previously mentioned, an aperiodic region is evident around the second coupled natural frequency at around 26 rad/s, where a gradient of peak amplitudes is present for the given forcing frequency. It follows from the bifurcation diagram shown in Figure 11 that no grazing bifurcation takes place for this configuration. In addition, it is clear that the first resonant peak (around 24 rad/s) has a nonlinear hardening effect which is mostly dominant by the primary structure response. On the other hand, the second peak is mostly dominated by the energy harvesting absorber. The nonlinear interaction between the energy harvester's motion and the stoppers results in the presence of these aperiodic responses. It should be mentioned that a nonlinear weak hardening effect also takes place for the second peak due to high interaction between the motion of the absorber and the stoppers. Also, due to the identical stiffnesses and gaps for both stoppers, a symmetry in the bifurcation diagram is obtained.

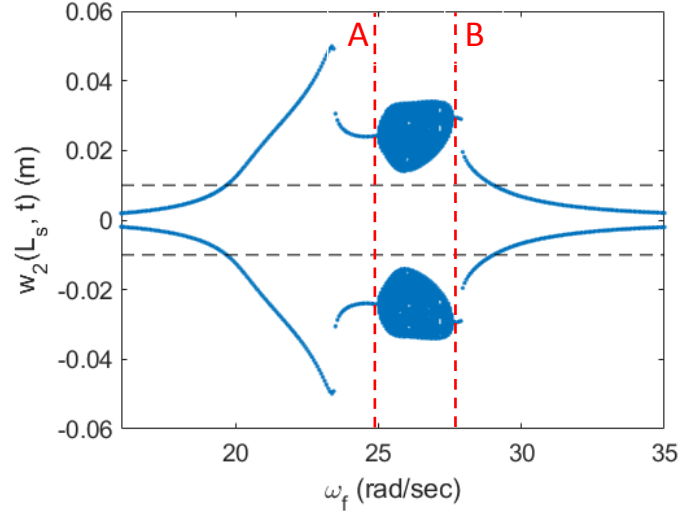


Figure 11: Bifurcation diagram of the energy harvesting absorber's motion versus the excitation frequency.

To better understand the types of aperiodic responses between the bifurcations at A and B shown in Figure 11, the time histories, phase portraits, power spectra, and Poincare maps before and after each transition are shown in Figures 9 and 10. Before the transition A, the plotted time history in Figure 12(a) indicates that the energy harvesting absorber is oscillating periodically. After the transition A, when carefully looking at the time history alone in Figure 12(b), it is quite possible to misrepresent the system's behavior. It appears that the system is behaving periodically with an order of 11 in the time history, but when looking at the Poincare map in Figure 12(h), a continuous closed loop is seen, thus indicating quasiperiodic behavior and the necessity of investigating the Poincare maps. Concerning the transition at bifurcation B, as depicted in Figure 13, it follows from the plotted time histories, phase portraits, power spectra, and Poincare maps that there is a change in the system's periodicity from an aperiodic motion to a periodic one. Prior to the bifurcation B, the Poincare map shown in Figure 13(g) indicates that the energy harvesting absorber is behaving quasiperiodically, as shown in Figure 13. After the bifurcation B, the absorber returns to periodic motion. It can be noted from the power spectra plots in Figures 10(e, f) that higher order superharmonics are activated prior to bifurcation B. After the bifurcation, only superharmonics of order 2 and 3 are present. As mentioned earlier, in the time histories and the phase portraits for both bifurcations A and B, it is clear that the grazing bifurcation is not present. The absorber is travelling 2 cm into the stopper before returning to its orbit. This is due to the stopper's stiffness being relatively low.

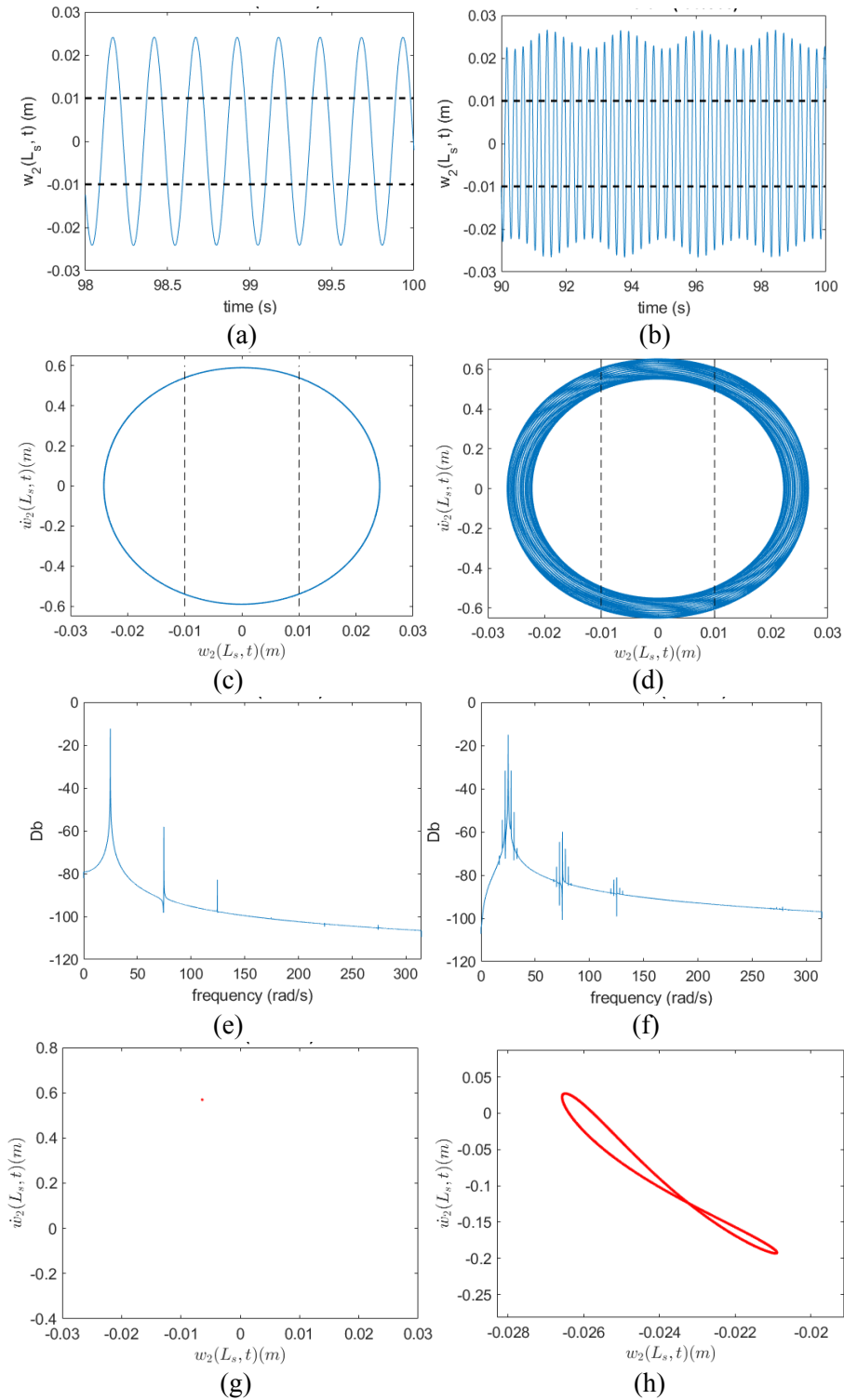


Figure 12: Bifurcation analysis at bifurcation A, where the first column represents the system's response before the bifurcation, and the second column represents the system's response after the bifurcation. (a, b) are the time histories, (c, d) are phase portraits, (e, f) are the power spectrum, and (g, h) are Poincare maps.

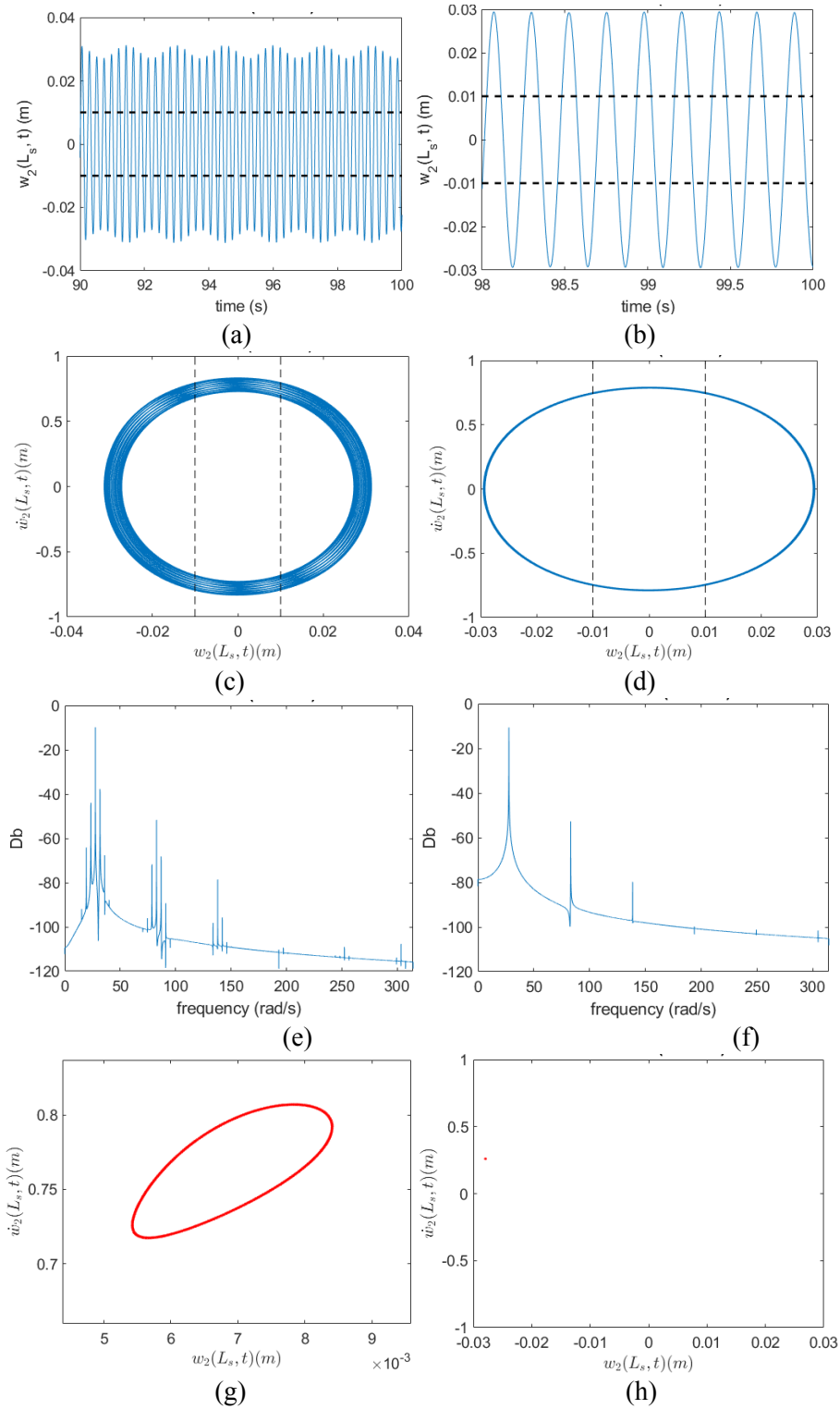


Figure 13: Bifurcation analysis at bifurcation B, where the first column represents the system's response before the bifurcation, and the second column represents the system's response after the bifurcation. (a, b) are the time histories, (c, d) are phase portraits, (e, f) are the power spectra, and (g, h) are the Poincaré maps.

4.2.2. Energy harvesting absorber's nonlinear characterization under hard stoppers configuration

As shown in the frequency response functions results in Section 4.1, stronger interaction between the energy harvesting absorber and the stoppers takes place when the stoppers' stiffnesses are high and the initial gap is small. In this section, a nonlinear characterization using nonlinear methods of nonlinear dynamics is carried out when the stoppers' stiffness is equal to $5 * 10^7 N/m$ and the gap size is set equal to $0.01 m$. The corresponding frequency response functions of the RMS primary structure and average harvested power were plotted in Figures 7(c) and 7(d), respectively. It was demonstrated that higher nonlinear interaction takes place between the energy harvesting absorber, stoppers, and primary structure with the presence of aperiodic responses for the energy harvesting absorber and high amplitudes of the primary structure. The bifurcation diagram for the energy harvesting absorber motion is plotted in Figure 14. The hard stoppers have a more dominant effect on the absorber compared to the results shown in Figure 12 for the medium stoppers configuration. This is seen when the energy harvesting absorber's motion nearly stops increasing once it contacts the stoppers. Unlike the medium stoppers, the hard stoppers are causing aperiodic regions around both coupled natural frequencies. Inspecting the bifurcation diagram shown in Figure 14, four different transitions can be identified. Two of them are associated with the first peak which is mostly dominated by the resonance of the primary structure and the other two are mostly related to the resonant frequency dominant by the energy harvesting absorber motion. It is obvious the second resonant peak is more affected by the hardness of the stoppers which results in an ultra-wide bandwidth resonance region with strong aperiodicity.

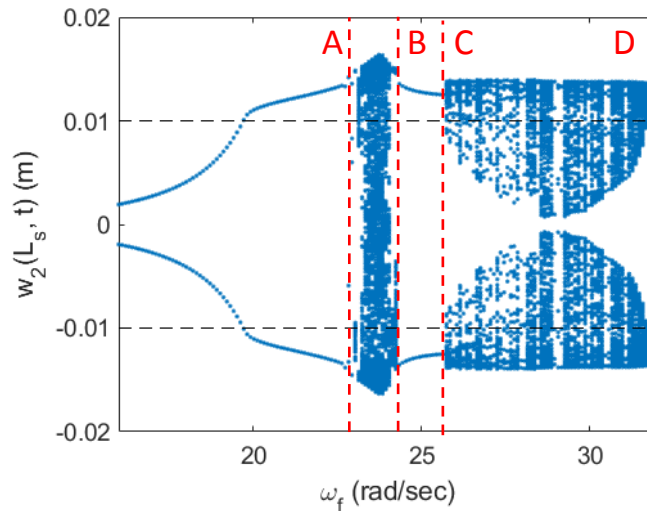
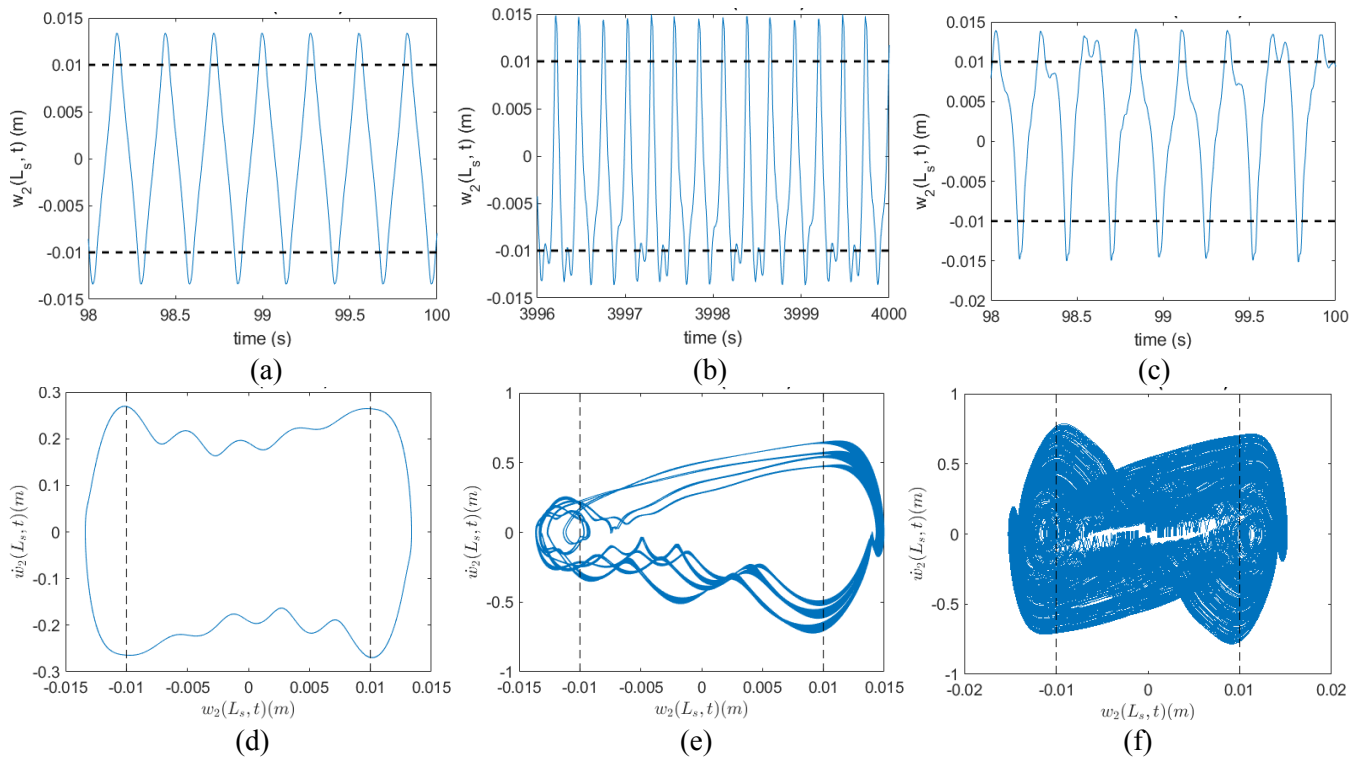


Figure 14: Bifurcation diagram of the energy harvesting absorber's motion versus the forcing frequency when hard stoppers are considered.

Starting with understanding the transition at bifurcation A, time histories, phase portraits, power spectra, and Poincare maps for three excitation frequencies before, during, and after the transition for the energy harvesting absorber motion are presented in Figure 15. It is clear that the absorber motion is periodic before

the bifurcation, as shown in Figure 15(a). During the transition, there is an onset of grazing bifurcation. This can be seen in the phase portrait in Figure 15(e), where the period is tangent with the left stopper constraint. From the power spectrum, depicted in Figure 15(h), it can be seen a dominant frequency Ω and $\frac{9}{8}\Omega$, indicating that the period of the system is $\frac{f}{8}$, meaning the system is of period-8. This is also indicated by the 8 distinct dots in the Poincare map in Figure 15(k). The absorber motion then transitions to chaotic behavior after the bifurcation, indicated by the infinite random distribution in the Poincare map in Figure 15(l). The grazing bifurcation is still present after the bifurcation, but the higher forcing frequency causes the absorber to behave chaotically. These results show the complexity of designing an energy harvesting absorber with hard stoppers which negatively affects the effectiveness of the energy harvester and the control of the primary structure. It should be mentioned that an ultra-wide bandwidth resonance region takes place, but little amount of power can be generated. Also, this hard impact may result in the fatigue of the energy harvester and hence its lifetime performance decay.



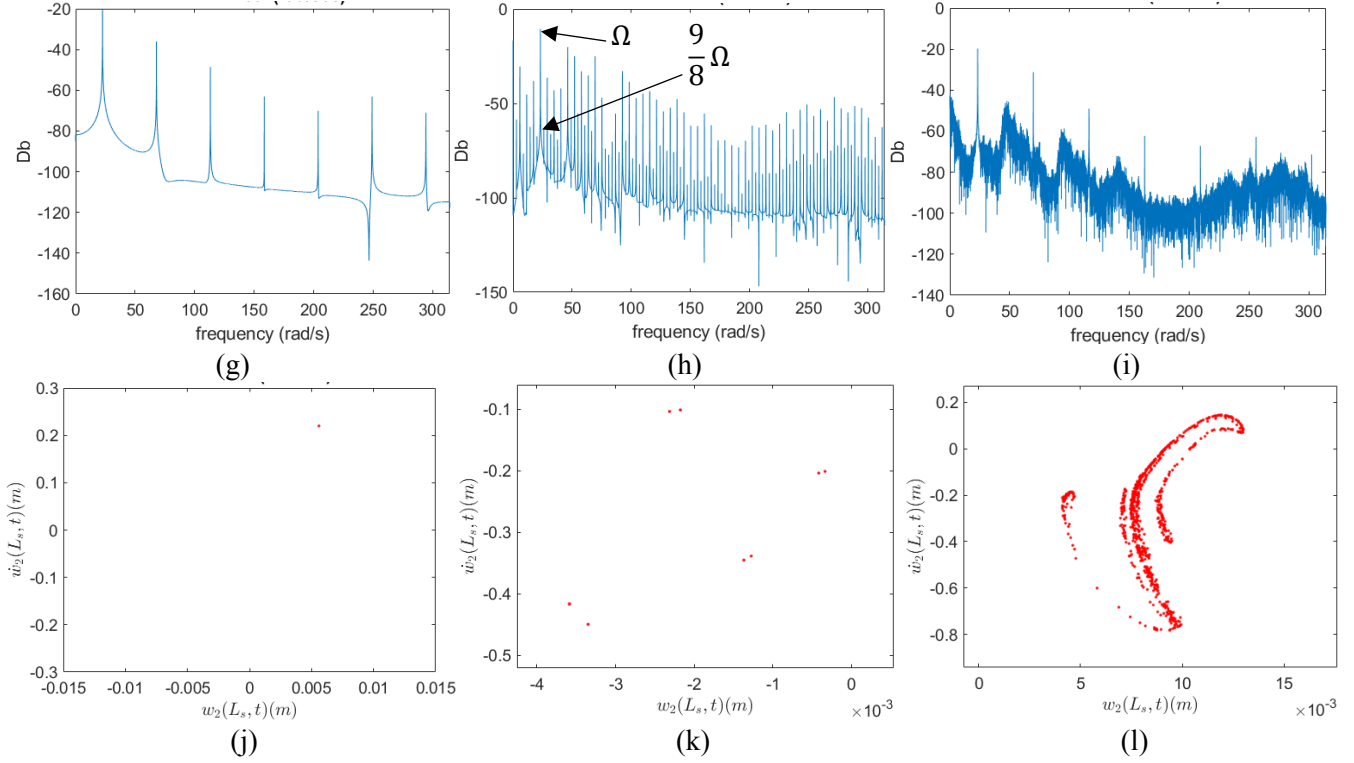


Figure 15: Bifurcation analysis of bifurcation A, where the first column represents the system's response before the bifurcation, the second column represents the system's response during the bifurcation, and the third column represents the system's response after the bifurcation. (a, b, c) are the time histories, (d, e, f) are phase portraits, (g, h, i) are power spectrum, and (j, k, l) are Poincaré maps.

The impacts of the hard stoppers on the energy harvesting absorber motion at the end of the chaotic response marked by bifurcation B in Figure 14 are investigated. Indeed, the plotted time histories, phase portraits, power spectra, and Poincaré maps for the motion of the energy harvester before and after this transition are shown in Figure 16. Before transition B, the energy harvesting absorber motion is showing a near grazing bifurcation (Figure 16(c)) with the dominance of the quadratic nonlinearity. Indeed, the superharmonic of order 2 is activated in the power spectrum plot shown in Figure 16(e). Figure 16 Even though the time history is complex, the absorber is still behaving periodically, seen with the single cycle in the phase portrait (Figure 16(c)) and the single point in the Poincaré map (Figure 16(g)). It is assumed that the presence of the near-grazing bifurcation makes the system stable compared to the previous chaotic behaviors when the grazing bifurcation was present. After Bifurcation B, the absorber is still behaving periodically, but it is calm compared to the behavior before the bifurcation. Additionally, it is apparent in the power spectrum plots that the superharmonic of order 2 is no longer present, which could be the cause of the bifurcation occurring. This bifurcation shows the dominance of the quadratic or cubic nonlinearity depending on the vibro-impact motion

between the energy harvesting absorber and stoppers. In fact, the activation of the superharmonic of order 2 results in the presence of the near grazing bifurcation.

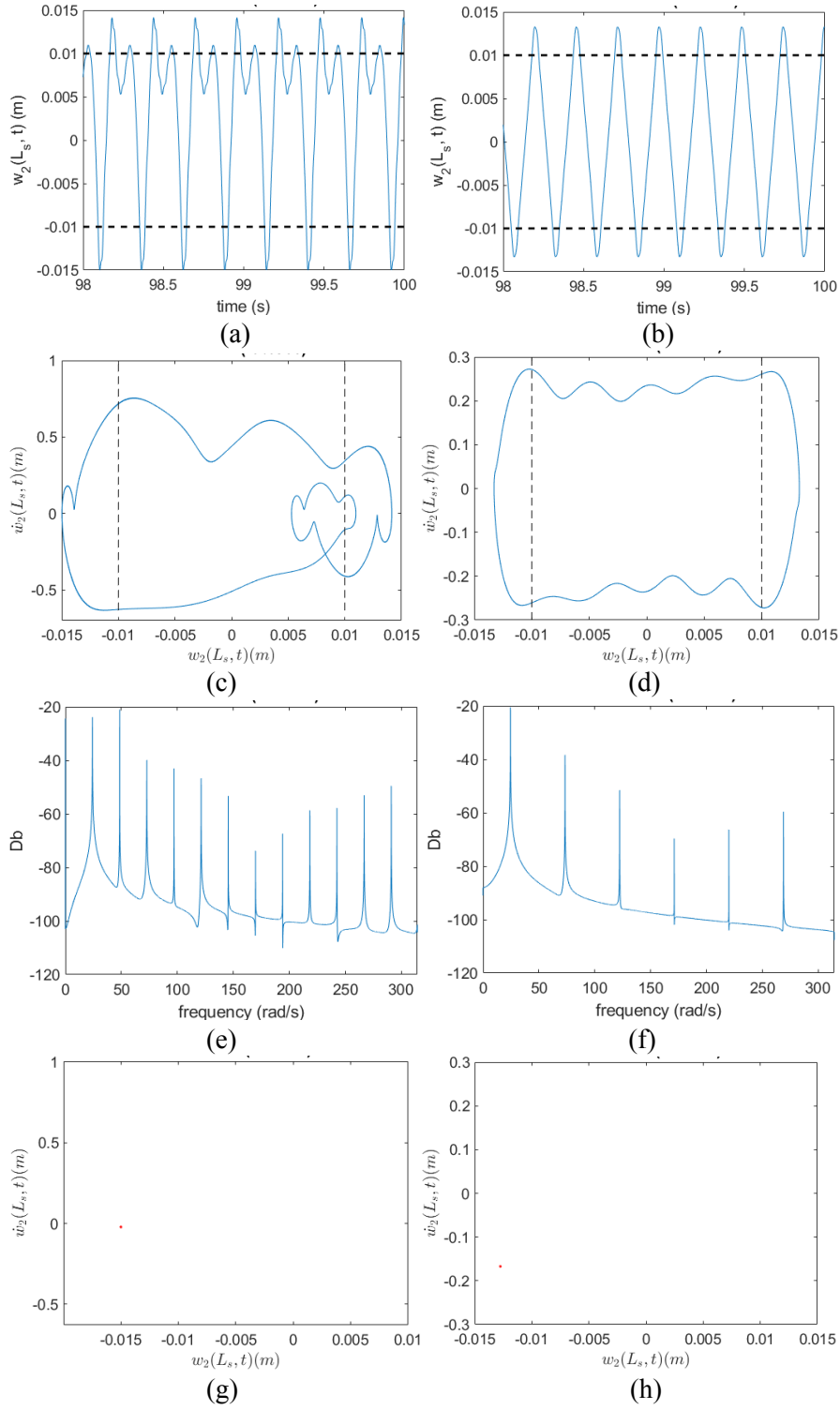
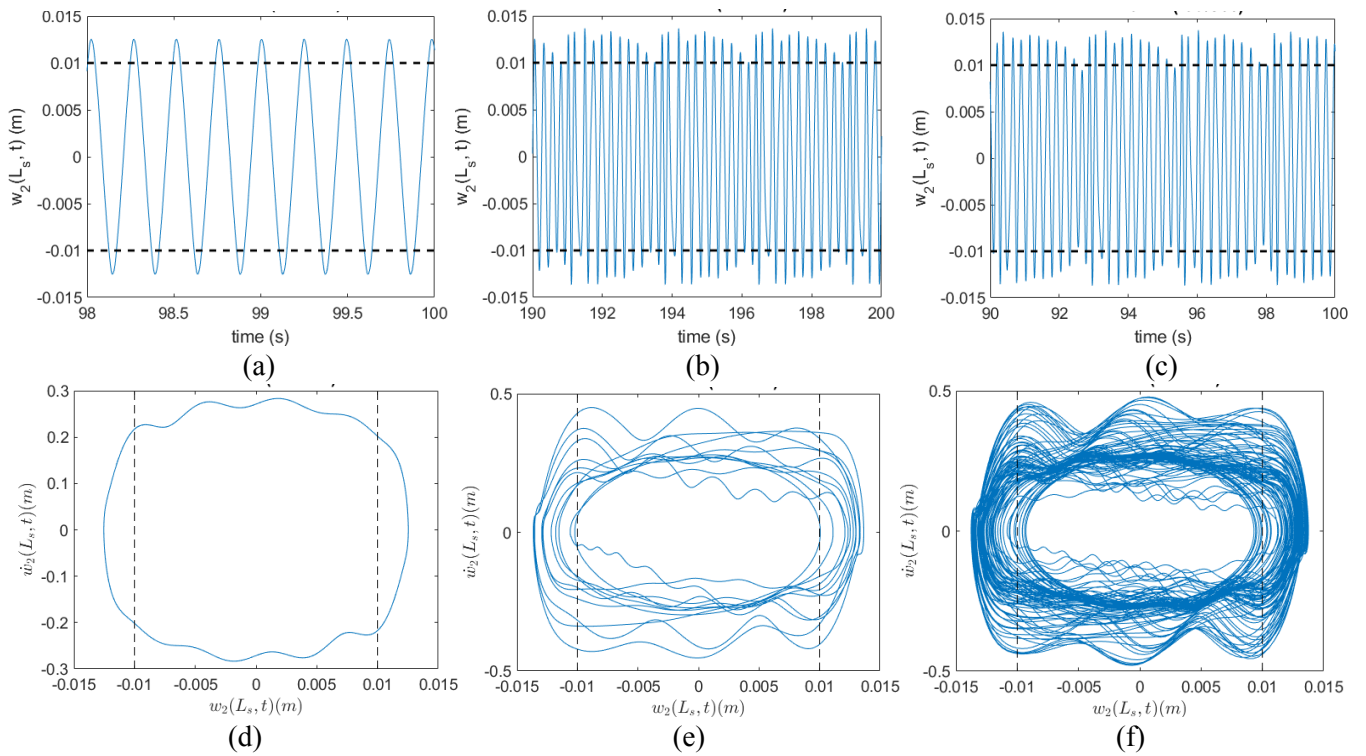


Figure 16: Bifurcation analysis of Bifurcation B, where the first column represents the system's response before the bifurcation, and the second column represents the system's response after the bifurcation. (a, b) are the time histories, (c, d) are phase portraits, (e, f) are the power spectra, and (g, h) are Poincaré maps.

Next, an investigation is performed on the dynamics of the energy harvesting absorber when the excitation frequency is near the coupled frequency dominated by the absorber response. Figure 17 presents the absorber's behavior before, during, and after bifurcation C. The time histories for during and after the bifurcation are extremely similar, thus proving the need to investigate the power spectra and Poincare maps. During the bifurcation, the energy harvesting absorber's behaves with period-11 response. This is also evident in the power spectrum where the first two dominant frequencies are Ω and $\frac{12}{11}\Omega$. The energy absorber then behaves chaotically after the bifurcation. This bifurcation is due to the presence of grazing bifurcation. During the bifurcation, grazing bifurcation is present while the absorber is behaving periodically and is also present in some periods of the chaotic behavior after the bifurcation. The importance of using the Poincare sections result is proved in characterizing the response of the energy harvester during and after bifurcation C. It is clear that due to the strong nonlinear effect of the hard stoppers, the harvester's motion transitions from periodic, to period-11, to chaotic.



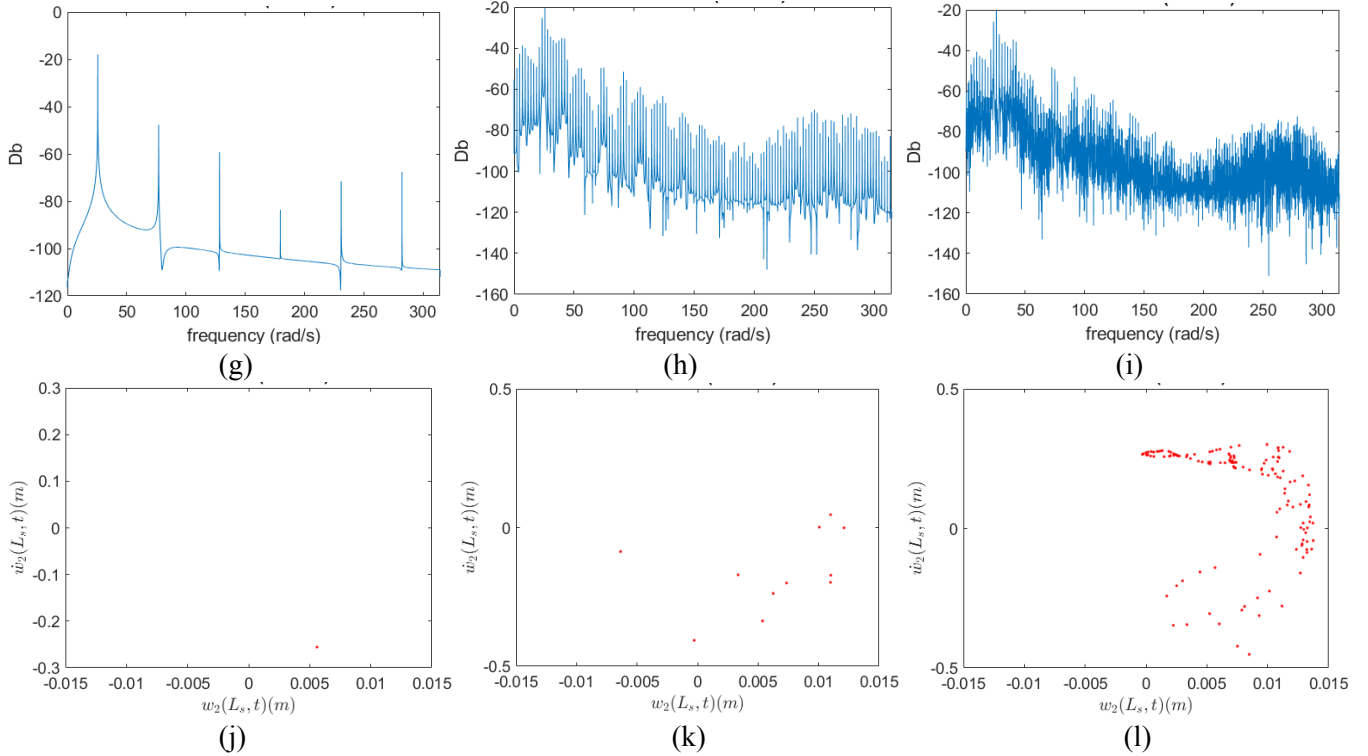


Figure 17: Bifurcation analysis of Bifurcation C, where the first column represents the system's response before the bifurcation, the second column represents the system's response during the bifurcation, and the third column is after the bifurcation. (a, b, c) are the time histories, (d, e, f) are phase portraits, (g, h, i) are the power spectra, and (j, k, l) are the Poincaré maps.

The characterization of the bifurcation D is carried out in Figure 18 where the impacts of the hard stoppers on the dynamical response of the energy harvester are determined before, during, and after the bifurcation. Inspecting the Poincaré map shown in Figure 18(j), it is obvious that the energy harvester absorber is behaving quasi-periodically before the bifurcation. During the transition, it follows from the Poincaré map presented in Figure 18(k) that the energy harvesting absorber is close to behaving quasi-periodically, seen as the chaotic nature of the points loosely form a closed loop. During the bifurcation, it can be seen in the phase portrait in Figure 18(e) that one orbit comes into contact tangentially with the stopper, indicating the possible presence of grazing bifurcation during this transition. After the bifurcation, the absorber oscillates periodically and there is no presence of superharmonic frequencies in the power spectrum due the absence of any contact with the stoppers. Clearly, aperiodic responses with different categories including period- n , quasiperiodic, and chaotic take place when the vibro-impact motion is present which lead the complexity of the dynamics of the energy harvesting absorber, a reduction in the levels of the harvested power, an increase in the amplitude of the primary structure and its aperiodicity.

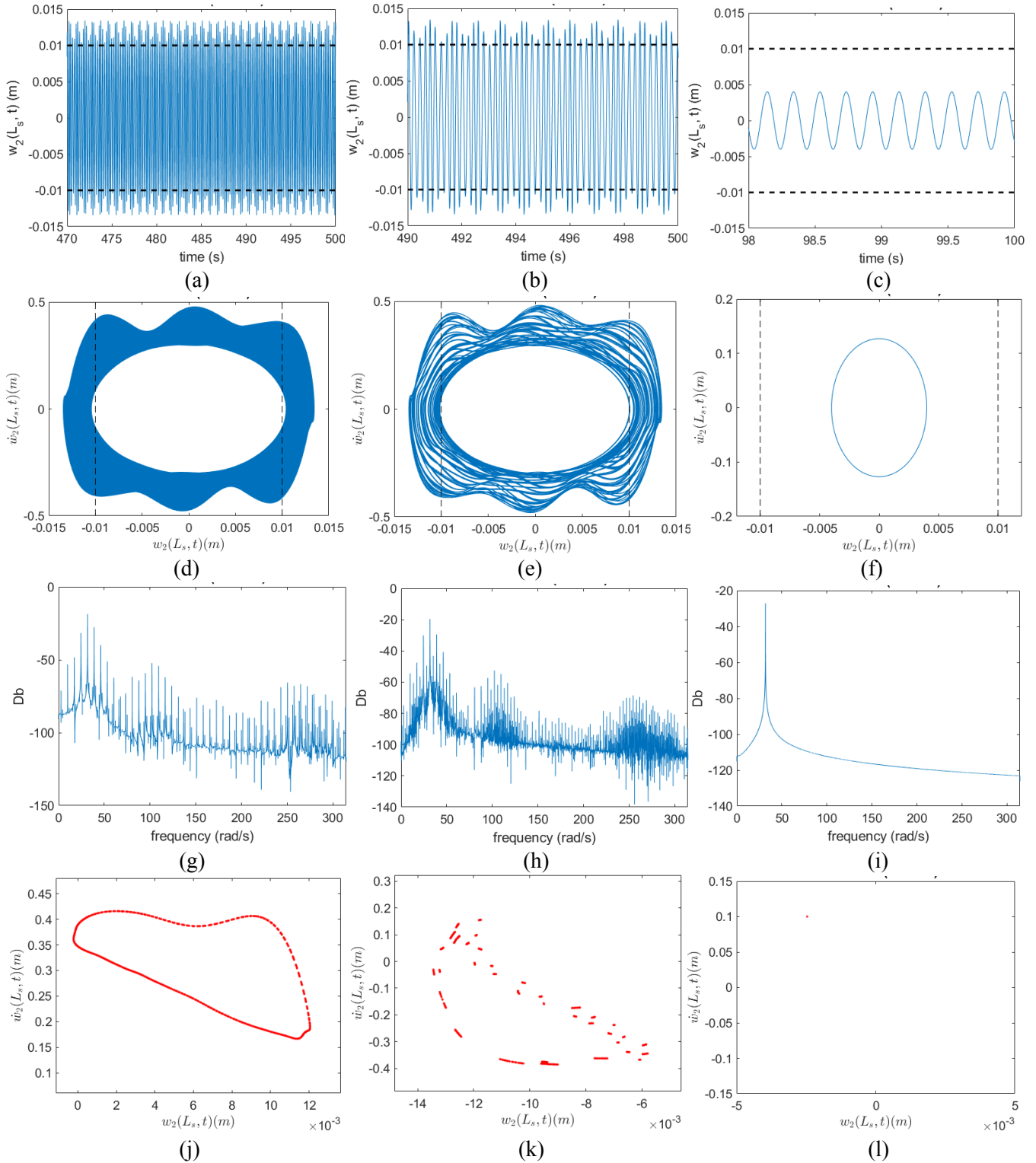


Figure 18: Bifurcation analysis of Bifurcation D, where the first column represents the system's response before the bifurcation, the second column represents the system's response during the bifurcation, and the third column is after the bifurcation. (a, b, c) are the time histories, (d, e, f) are the phase portraits, (g, h, i) are the power spectra, and (j, k, l) are the Poincaré maps.

As illustrated in the bifurcation diagram shown in Figure 14, the second aperiodic region bounded by bifurcations C and D is a complex region and should be explored and characterized in a deeper way. A closer look at this region is depicted in Figure 19. Inspecting this figure, it is clear that several transitions take place depending on the nonlinear interaction between the energy harvesting absorber and the hard stoppers. These multiple bifurcations in this region appear to follow a pattern, switching between chaos and a stable period of period- n .

To find the source of this pattern, the periodic region denoted by bifurcations E and F is investigated in Figure 20. In this figure, the behavior of the energy harvesting absorber is characterized before and during bifurcation E, during the stable region, and during and after bifurcation F. The Poincare maps plot in Figure 20(d) shows that the stable regions are of period-9, denoted by the nine distinct black points. At all other locations throughout the bifurcations the absorber is behaving quasi-periodically. When looking at the time histories and the phase portraits in Figures 17(a) and 17(b), respectively, it is clear that these bifurcations are caused by the presence of a grazing bifurcation. The phase portrait during the periodic region shows that the absorber is orbiting very closely to the amplitude stoppers. During bifurcations E and F, the energy harvesting absorber can be seen to tangentially meet the stoppers. The absorber is sent into chaos when the absorber grazes the stoppers, until it degenerates back to a periodic behavior.

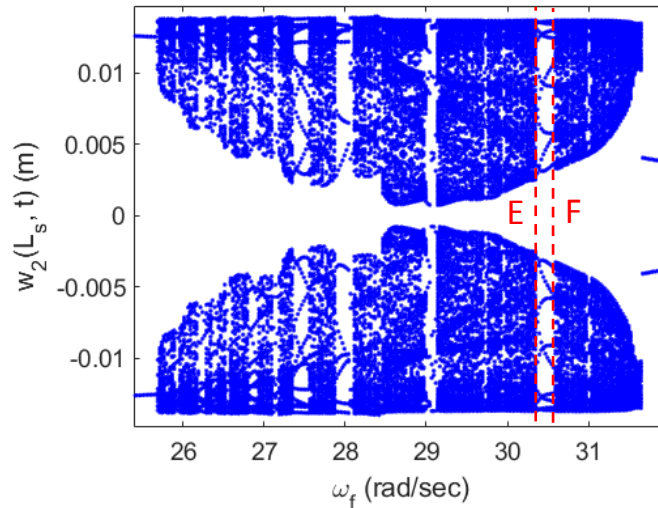


Figure 19: Bifurcation diagram of the second aperiodic region in the absorber's amplitude versus the forcing frequency.

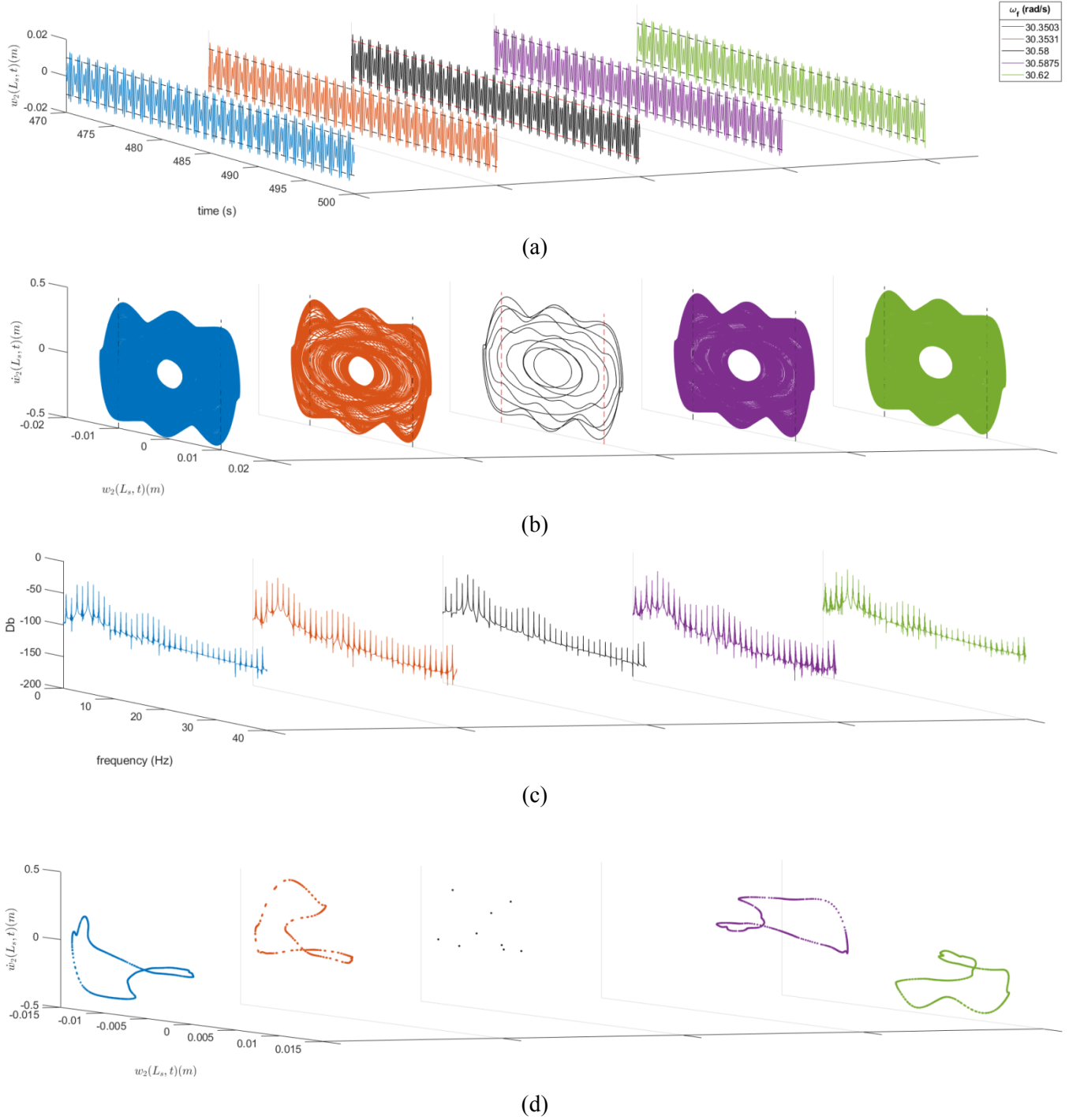


Figure 20: Characterization of the transitions between bifurcation E and F: (a) time histories, (b) phase portraits, (c) power spectra, and (d) Poincaré maps.

5. Conclusions

An energy harvester with amplitude stoppers was utilized as a tuned-mass-damper to control a dynamical system under base excitation. Both Euler-Bernoulli beam theory and Galerkin discretization were employed

to derive a nonlinear reduced-order model for the primary structure and the energy harvester. A linear analysis was performed to optimize the energy-harvesting absorber's parameters to control the primary structure's oscillations and simultaneously harvest energy over a broadband resonance region. Three categories of amplitude stoppers stiffnesses were investigated, namely, soft, medium, and hard. The results showed that the soft stiffness adequately affected the behavior of the coupled system through a great transfer of energy between the primary structure and the energy harvesting absorber. The soft stoppers also showed promising control of the primary structure, significant increase of peak power, and little improvement in broadband region of the harvested power. Medium stiffnesses also had an increase in generated power, but an aperiodic region developed around the second coupled natural frequency took place. Hard stiffnesses resulted in a decrease in the peak power and did not show control of the primary structure. The aperiodic regions in the medium and hard stiffnesses were developed by the presence of grazing bifurcation, causing a change from period- n or quasiperiodic behavior to transition into chaotic behavior and vice versa.

Acknowledgments

Tyler Alvis would like to thank Brian Saunders for his continued support and guidance throughout the nonlinear characterizations of the system. The authors would like to thank Sandia National Laboratories for their continued support and funding of this research. Sandia National Laboratories is a multi-mission laboratory managed and operated by National Technology and Engineering Solutions of Sandia, LLC, a wholly owned subsidiary of Honeywell International Inc., for the U.S. Department of Energy's National Nuclear Security Administration under contract DE-NA0003525.

References

- [1] Ono, K., Kasai, H., & Sasagawa, M. (1996). Up-down vibration effects on bridge piers. *Soils and foundations*, 36, 211-218.
- [2] United States. Bureau of Mines, & Siskind, D. E. (1980). *Structure response and damage produced by ground vibration from surface mine blasting* (p. 74). New York, NY, USA: US Department of the Interior, Bureau of Mines.
- [3] Chopra, A. K. (1995). *Dynamics of Structures: Theory and Applications to Earthquake Engineering*, Prentice Hall. Inc., Upper Saddle River, NJ.
- [4] Willsky, A. S. (1976). A survey of design methods for failure detection in dynamic systems. *Automatica*, 12(6), 601-611.
- [5] Muthalif, A. G., & Nordin, N. D. (2015). Optimal piezoelectric beam shape for single and broadband vibration energy harvesting: Modeling, simulation and experimental results. *Mechanical Systems and Signal Processing*, 54, 417-426.
- [6] Tokhi, M. O., & Hossain, M. A. (1994). Self-tuning active vibration control in flexible beam structures. *Proceedings of the Institution of Mechanical Engineers, Part I: Journal of Systems and Control Engineering*, 208(4), 263-278.

- [7] Zhang, S. Y., Jiang, J. Z., & Neild, S. A. (2017). Passive vibration control: a structure–immittance approach. *Proceedings of the Royal Society A: Mathematical, Physical and Engineering Sciences*, 473(2201), 20170011.
- [8] Bigdeli, Y., & Kim, D. (2016). Damping effects of the passive control devices on structural vibration control: TMD, TLC and TLCD for varying total masses. *KSCE Journal of Civil Engineering*, 20(1), 301-308.
- [9] Yokota, H., Saruta, M., Nakamura, Y., Satake, N., Okada, K., Ogawa, Y., & Fujita, Y. (1992). Structural control for seismic load using viscoelastic dampers. *Proc., 10WCEE*.
- [10] Hoang, N., Fujino, Y., & Warnitchai, P. (2008). Optimal tuned mass damper for seismic applications and practical design formulas. *Engineering structures*, 30(3), 707-715.
- [11] Marian, L., & Giaralis, A. (2014). Optimal design of a novel tuned mass-damper–inertor (TMDI) passive vibration control configuration for stochastically support-excited structural systems. *Probabilistic Engineering Mechanics*, 38, 156-164.
- [12] Poon, D., Shieh, S. S., Joseph, L. M., & Chang, C. (2004, October). Structural design of Taipei 101, the world’s tallest building. In *Proceedings of the CTBUH 2004 Seoul Conference, Seoul, Korea* (pp. 271-278).
- [13] Lu, Z., Chen, X., Zhang, D., & Dai, K. (2017). Experimental and analytical study on the performance of particle tuned mass dampers under seismic excitation. *Earthquake Engineering & Structural Dynamics*, 46(5), 697-714.
- [14] Gatti, G., Brennan, M. J., Tehrani, M. G., & Thompson, D. J. (2016). Harvesting energy from the vibration of a passing train using a single-degree-of-freedom oscillator. *Mechanical Systems and Signal Processing*, 66, 785-792.
- [15] Aljadiri, R. T., Taha, L. Y., & Ivey, P. (2017). Electrostatic energy harvesting systems: A better understanding of their sustainability. *Journal of Clean Energy Technologies*, 5(5), 409-416.
- [16] Saha, C. R., O'Donnell, T., Loder, H., Beeby, S., & Tudor, J. (2006). Optimization of an electromagnetic energy harvesting device. *IEEE Transactions on Magnetics*, 42(10), 3509-3511.
- [17] Kecik, K. (2018). Assessment of energy harvesting and vibration mitigation of a pendulum dynamic absorber. *Mechanical Systems and Signal Processing*, 106, 198-209.
- [18] Erturk A and Inman D J 2011 *Piezoelectric Energy Harvesting* (New York: Wiley)
- [19] Behrens, S., Fleming, A. J., & Moheimani, S. O. R. (2003). A broadband controller for shunt piezoelectric damping of structural vibration. *Smart materials and structures*, 12(1), 18.
- [20] Moheimani, S. R., & Fleming, A. J. (2006). *Piezoelectric transducers for vibration control and damping*. Springer Science & Business Media.
- [21] Harne, R. L. (2013). Development and testing of a dynamic absorber with corrugated piezoelectric spring for vibration control and energy harvesting applications. *Mechanical Systems and Signal Processing*, 36(2), 604-617.
- [22] Abdelmoula, H., & Abdelkefi, A. (2016). The potential of electrical impedance on the performance of galloping systems for energy harvesting and control applications. *Journal of Sound and Vibration*, 370, 191-208.
- [23] Abdelmoula, H., Dai, H. L., Abdelkefi, A., & Wang, L. (2017). Control of base-excited dynamical systems through piezoelectric energy harvesting absorber. *Smart Materials and Structures*, 26(9), 095013.
- [24] McNeil, I., & Abdelkefi, A. (2021). Nonlinear modeling and vibration mitigation of combined vortex-induced and base vibrations through energy harvesting absorbers. *Communications in Nonlinear Science and Numerical Simulation*, 95, 105655.
- [25] Zhou, K., Dai, H. L., Abdelkefi, A., Zhou, H. Y., & Ni, Q. (2019). Impacts of stopper type and material on the broadband characteristics and performance of energy harvesters. *AIP Advances*, 9(3), 035228.
- [26] Zhou, K., Dai, H. L., Abdelkefi, A., & Ni, Q. (2020). Theoretical modeling and nonlinear analysis of piezoelectric energy harvesters with different stoppers. *International Journal of Mechanical Sciences*, 166, 105233.

- [27] Abdelkefi, A., & Barsallo, N. (2014). Comparative modeling of low-frequency piezomagnetoelastic energy harvesters. *Journal of Intelligent Material Systems and Structures*, 25(14), 1771-1785.
- [28] Paidoussis, M. P., Li, G. X., & Rand, R. H. (1991). Chaotic motions of a constrained pipe conveying fluid: comparison between simulation, analysis, and experiment.
- [29] Hajjaj, A. Z., Alcheikh, N., & Younis, M. I. (2017). The static and dynamic behavior of MEMS arch resonators near veering and the impact of initial shapes. *International Journal of Non-Linear Mechanics*, 95, 277-286.
- [30] Vasconcellos, R., Abdelkefi, A., Hajj, M. R., & Marques, F. D. (2014). Grazing bifurcation in aeroelastic systems with freeplay nonlinearity. *Communications in Nonlinear Science and Numerical Simulation*, 19(5), 1611-1625.
- [31] Yan, Z., & Abdelkefi, A. (2014). Nonlinear characterization of concurrent energy harvesting from galloping and base excitations. *Nonlinear Dynamics*, 77(4), 1171-1189.